Hindawi
Advances in Civil Engineering
Volume 2023, Article ID 7596032, 25 pages
https://doi.org/10.1155/2023/7596032

Research Article

Post-Earthquake Fire Punching Shear Behavior of GFRP-Reinforced Slab-Column Connections

Tesfaye Alemu Mohammed [1,2] **and Shewarega Shirtaga** [2]

[1]*Construction Quality and Technology Center of Excellence, Addis Ababa Science and Technology University, Addis Ababa, Ethiopia*
[2]*Department of Civil Engineering, Addis Ababa Science and Technology University, Addis Ababa, Ethiopia*

Correspondence should be addressed to Tesfaye Alemu Mohammed; tes.alemu@gmail.com

Received 18 July 2022; Revised 15 January 2023; Accepted 4 February 2023; Published 23 February 2023

Academic Editor: Zhongguo John Ma

It is not uncommon for reinforced concrete slab-column assembly to experience a punching brittle shear failure type under seismic loading. This research work numerically investigates the punching shear behavior of interior GFRP-reinforcedslab-column connections under post-earthquake fire. Two experimental results reported in the article were used for validation analysis using ANSYS nonlinear finite element software program. Further, parametric studies on influential variables such as fire exposure duration, concrete grade, slab thickness, fire exposed surface, and column aspect ratio were performed to get insight into the post-earthquake fire behavior of GFRP-reinforcedslab-column connections. Finite element analysis results showed decreasing fire exposure duration, enhancing grades of concrete, increasing slab thickness, minimizing fire exposure surfaces, and increasing column aspect ratio, which improved the punching shear capacity of GFRP-reinforced slab columns. Moreover, increasing slab thickness provided good performance against post-earthquake fire loading as compared to enhancing concrete grades in GFRP-reinforcedslab-column assemblies. The research concludes that it is crucial to take post-earthquake fire into account when designing structures to ensure no collapse safety design requirements.

1. Introduction

Slab-column connections, also known as flat slab constructions, are assemblies of a building in which reinforced concrete floor slabs are directly attached to columns without the use of beams. Flat slab constructions are popular in residential buildings and car parking garages partly due to their advantages, such as reduced story heights, flat finishes, fast construction times, and flexibility to put columns in a variety of positions [1]. However, despite the aforementioned advantages of flat slab construction, there is also a risk that a hazardous brittle failure mode, namely, punching shear failure, is likely to occur if shear stresses in the floor reach critical levels and a RC column punches through a slab (Figure 1). The main cause of this failure is a load being transferred directly to a column in shear through a relatively small area of concrete [1].

As opposed to conventional steel rebars, glass fiber-reinforced polymer (GFRP) has immunity against corrosion, light self-weight, and high tensile strength. This characteristics appeal for its use as an alternative construction material [2]. In contrary, GFRP rebars have lower elastic stiffness, resulting in a lower punching shear capacity of GFRP-RC slab-column connections as compared to corresponding steel rebar counter parts with the same steel reinforcement ratio [2], and despite this, GFRP rebars have been shown to resist seismic loads in slab-column connections [3].

Recent studies [4–6] investigated the punching shear behavior of interior FRP-RC slab-column connections with various forms of FRP shear reinforcement under monotonic load. Similarly, few researchers [3, 7–9] studied the effectiveness and contribution of GFRP stirrups as shear

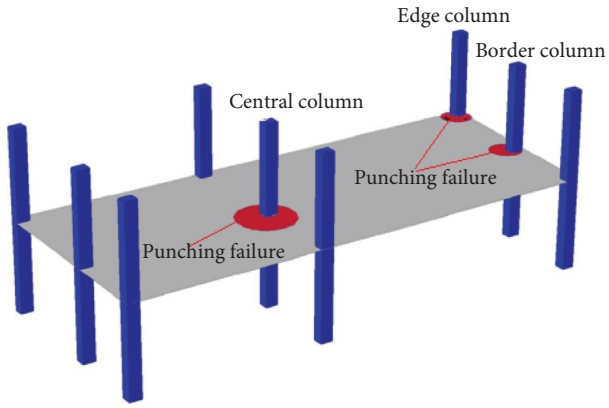

Figure 1: Flat plate.

reinforcement in two-way slabs under lateral cyclic load. Their findings revealed that the use of GFRP stirrups resulted in a more flexible punching shear failure mechanism.

Numerous studies [1–9] investigated the punching shear behavior of GFRP-reinforcedslab-column connections at ambient temperatures, and there is perceived void in the article on post-earthquake fire punching shear behavior of GFRP-reinforcedslab-column connections. Secondary fire loading followed by an earthquake action poses a major threat to structural integrity of a member and needs in detail study as a structural member's singular response for only fire, and only earthquake is different as compared to combined post-earthquake fire scenario [10].

Prior studies on structural responses to fire have primarily focused on steel members, RC flat slabs, RC columns, and RC beams. However, it ignored the GFRP-reinforcedslab-column connection that was exposed to post-earthquake fire. Long-termpost-earthquake fire exposure can result in significant thermal gradients through the GFRP-reinforcedslab-column connections, which could eventually cause punching failure of the connections under post-earthquake fire loading conditions. By presenting numerical modeling of a GFRP-reinforcedslab-column connection subjected to the post-earthquake fire, this research fills in a significant knowledge gap on the subject. This information may ultimately contribute to the improvement of analysis tools for the rational load-based design of GFRP-reinforced concrete structures under post-earthquake fire loading.

The present research work fills in perceived void in the article by studying post-earthquake fire punching shear behavior of GFRP-reinforcedslab-column connections. Two experimental data reported in recent articles [3, 11] were used for validation and verification of developed 3D FE models using the ANSYS nonlinear finite element software program. Further, parametric studies were performed on influential variables such as post-earthquake fire exposure duration, concrete grade, slab thickness, fire exposed surface, and column aspect ratio to get insight into the punching shear behavior of GFRP-reinforcedslab-column connections subjected to post-earthquake fire loading.

2. Materials and Methodology

Post-earthquake fire was modeled using ANSYS [12] coupled-field analysis methodology. Solutions and procedures associated with a particular engineering discipline are referred to as coupled-field physics analyses when the input of one physics analysis depends on the results of another analysis. The complete analyses are defined as coupled-field analysis. Thus, a sequentially coupled thermal-stress analysis is conducted in ANSYS in view of the fact that the stress/displacement solution is dependent on a temperature field, but there is no inverse dependency.

Coupled-field analysis involves a sequential analysis where first fire loading is applied and finite element analysis is performed to evaluate nodal temperatures of a FE model. This is followed by the application of structural loading and the execution of finite element analysis to evaluate the residual strength, stress, and deformation of a structure. This coupled-field sequential analysis shows the response of a structure subjected to post-earthquake fire [12].

Since there are no reported experimental works on punching shear behavior of slab subjected to post-earthquake fire, the authors of this study used two experimental works reported in the article for the validation and verification of developed FE models. One experimental work is on GFRP-reinforcedslab-column connection subjected to lateral loading [3], and the second experimental work is on reinforced concrete flat slab subjected to fire loading [11]. When combined, the aforementioned two cases characterize the behavior of RC slab under a post-earthquake fire scenario. In coming sections, details of the two experimental works employed for validation and verification FEA are presented.

2.1. Description of Part-I Specimen for FE Model Validation and Verification: GFRP-ReinforcedSlab-Column Connection under Lateral Cyclic Loading. Interior GFRP-reinforcedslab-column connection with GFRP shear reinforcement provided at 2 d from the face of a column, experimentally tested by [3] under reversed cyclic loading, was selected for validation and verification FEA of earthquake loading. This adequately designed GFRP-reinforcedslab-column connection specimen was also used as a control specimen.

Experimental tests were conducted by [3] for shear-governedslab-column connections reinforced with glass fiber-reinforced polymer bars constructed without and with GFRP shear reinforcement. From these tested specimens, slab-column connections with GFR shear reinforcement were used to capture the effects of shear reinforcement as well as other investigated parameters for NLFEA. Also, from this shear reinforcement, provided slab-column connections used to provide shear reinforcement up to 2 d from the face of columns, this specimen is collapsed at 4.5% drifts, so we use this to capture the computational times of NLFEA compared to others shear reinforcement slab-column connection sample.

2.1.1. Details of Part-I Specimen. The geometry and reinforcement detailing characteristics of the developed FE model were identical to experimental work conducted by [3] on full-scaleGFRP-reinforcedslab-column connections with GFRP shear reinforcement provided at 2 d from the face of the column. The slab-column connection has a geometric dimension of 2500 mm × 2500 mm with a thickness of 200 mm and a 300 mm square column, extending 700 mm above and below slab surfaces (Figure 2). Sand-coated GFRP reinforcing bars (10 no. 15 and 14 no. 20) were used for flexural reinforcement at top and bottom of a slab, whereas closed GFRP shear reinforcement (16 no. 10) was also used in the slab. Moreover, six longitudinal deformed steel bars (25 M) and 16 closed ties (10 M) were used in columns. The reinforcement configurations of the specimen are shown in Figure 2 with bottom and top reinforcement placed symmetrically in each orthogonal direction.

2.1.2. Material Properties of Part-I Specimen. Material properties employed for FE models were similar to experimental works conducted by [3] on full-scaleGFRP-reinforcedslab-column connections. Elastic module values of both bottom and top GFRP flexural reinforcements of a slab were 64.9 and 62.6 GPa, respectively, whereas elastic modulus of the GFRP shear reinforcement for the slab is 45 GPa. The yield strength of the main steel column rebar and steel column shear reinforcement was 4706 MPa and 2806 MPa, respectively. A compressive strength of concrete used for both slab and column was 45 MPa. Detailed material properties of concrete, GFRP, and steel rebar reinforcement are shown in Table 1.

2.2. Finite Element Modeling of Part-I Specimen Using ANSYS Software Program

2.2.1. Element Types. CPT215 element type from ANSYS element library was used to model the concrete and steel loading plates. CPT215 element is a brick element with eight nodes and has three degrees of freedom per nodes. The element has the capability of stress stiffening, large deflection, elasticity, and large strain [12].

Reinf264 element from ANSYS element library was employed to model steel and GFRP reinforcement. Reinf264 element is a uniaxial tension and compression element with two nodes. Reinf264 element has three translational degrees of freedom compatible with the parent concrete CPT 215 element [12]. This element is also capable of simulating nonlinearity and plastic deformations.

2.2.2. Material Types. A coupled damage-plasticity microplane model from ANSYS material library was used to model concrete material. A coupled damage-plasticity microplane model was formulated from research works of [13–15], where concrete material is characterized through uniaxial stress-strain laws of various individual planes [12].

For the concrete, a coupled regularized damage-plasticity microplane model was used [13]. In this model, uniaxial stress vs. strain equations are applied to several small planes, referred to as microplanes, to approximate the material behavior. This method was used to capture the concrete's inelastic behavior and get around the analysis's numerical instability caused by the material's strain softening [14]. A smooth, three-surface Drucker–Prager microplane with tension and compression cap surfaces serves as the definition for the coupled damage-plasticity microplane model. Limiting the yield surface's expansion in both tension and compression is the fundamental benefit of using two cap surfaces.

The use of a coupled damage-plasticity microplane model requires thirteen concrete material inputs out of which seven parameters are related to plasticity, four to damage, and two to nonlocal parameter. Parameters related to plasticity behavior of concrete includes Drucker–Prager yield function, compression cap, and hardening parameters [14, 15]. Drucker–Prager yield function parameters include listing of uniaxial compressive strength, biaxial compressive strength, and uniaxial tensile strength. The compression cap parameter listing refers to the abscissa intersection point between the compression cap and Drucker–Prager yield function and the ratio between the major and minor axes of the cap. Concrete plasticity hardening parameter listings are hardening material constant and tension cap hardening constant. The four damage parameter constants include tension and compression damage thresholds and tension and compression damage evolution constants. Last, two nonlocal parameters definition consisting of the nonlocal interaction range parameter and overnonlocal averaging parameter completes concrete material modeling using the coupled damage-plasticity microplane model. Table 2 presents details of concrete coupled damage-plasticity microplane model inputs for the Part-I FE model.

A bilinear isotropic and linear-elastic material model from ANSYS material library was used to characterize conventional steel rebars and GFRP reinforcement. Poisson's ratios of 0.3 and 0.25 were employed for the steel and GFRP bars, respectively. Modulus of elasticity and Poisson's ratio values of 200 GPa and 0.3 were used for steel loading plates material modeling. Table 1 presents detailed material inputs of steel rebars, GFRP flexural bars, and shear stirrups. A perfect bond was assumed between the concrete and embedded rebar reinforcements.

2.2.3. Model Geometry, Boundary Conditions, and Loading. Taking advantage of the symmetry, half of GFRP-reinforcedslab-column connection subassemblage was modeled using ANSYS mechanical APDL. Half of the entire model was considered in the longitudinal section of full interior slab-column connection. This approach leads to a reduction in computational time and storage disk space requirement.

A boundary condition was applied at the plane of symmetry and support locations to constrain nodes. At the plane of symmetry along x-axis, translation degree of freedom (DOF) in X -direction (U_x) was set to zero, and at

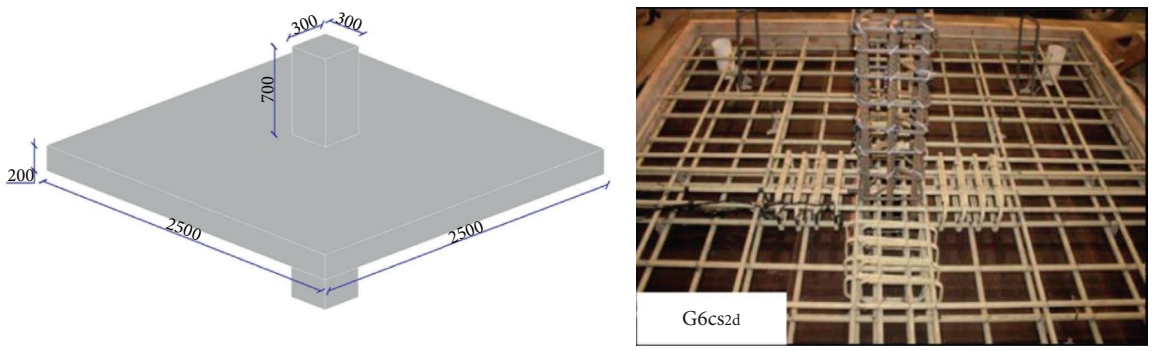

(a) (b)

Figure 2: Geometry and reinforcement configuration of part-I slab-column connection specimen [3]. (a) Geometry (mm). (b) Reinforcement detailing.

Table 1: Material properties of concrete, GFRP, and steel rebar reinforcement [3].

Materials							
Concrete	fc (MPa) 45	fct (MPa) 3.75					
Reinforcement type	Bar size	Bar Φ (mm)	Area (mm^2)	Elastic modulus (GPa)	Ultimate tensile strength (MPa)	Characteristics tensile strength (MPa)	Ultimate tensile elongation (%)
GFRP main slab	No. 15	15.9	199	62.6	1239	1184	1.89
bar	No. 20	19.1	285	64.9	1334	1079	2.07
Column steel bar	25 M	25.2	490	200	$F_u = 620$	$F_y = 470$	$\varepsilon y = 0.24$
Steel stirrup	10 M	11.3	100.2	200	—	280	—
GFRP stirrup	No. 10	9.49	71	45	948	504	0.53

Table 2: Concrete coupled damage-plasticity microplane model inputs.

Constant	Value
E (MPa)	36000
Nu	0.18
C1 (MPa)	45
C2 (MPa)	51.7
C3 (MPa)	3.8159
C4	1
C5	4000
C6	−31.5
C7	2
C8	0
C9	0.00002
C10	3000
C11	2000
C	1600
m	2.5

a support location similar to experimental set up [3], all translation DOF U_x, U_y, and U_z were set to zero. Moreover, identical to experimental set up [3], axial loading of 70 KN was applied at the top of a column to simulate gravity loading. Displacement-controlled FE analysis was performed by applying 60.75 mm of lateral displacement at a height of 675 mm from the center of a slab in the opposite direction on both top and bottom of columns. Figure 3 presents the loadings and boundary conditions of the developed FE model.

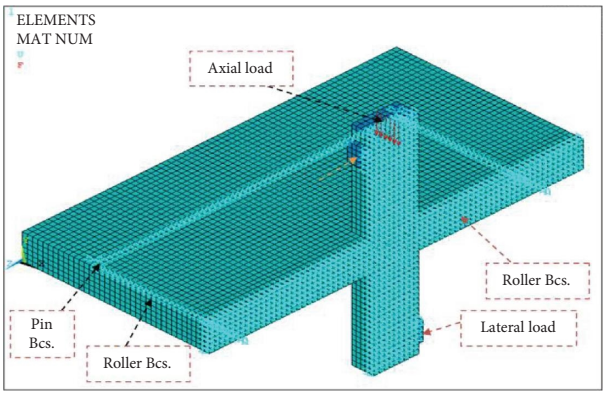

Figure 3: Geometry, meshing, loading, and boundary conditions of part-I specimen.

2.3. Description of Part-II Specimen for FE Model Validation and Verification: Punching Shear Strength of Reinforced Concrete Flat Slab Subjected to Fire Loading. In this section, experimental data reported by [11] on punching shear strength of reinforced concrete flat slab subjected to fire on their tension was chosen for validation and verification FEA of fire loading. This Part-II FE validation analysis complements the Part-I FE model validation on the application of fire loading. Details of the specimen are presented in the next few subsections.

2.3.1. Detailing of the Specimen. A full-scale RC flat slab specimen chosen for FE validation analysis on fire loading has width and length geometric dimensions of 1100×1100 mm. The flat slab has 100 mm thickness and a 150 mm square column extending 400 mm height above the flat slab surface. The flat slab was reinforced with 11 Φ 10 mm rebars in the tension side and 7 Φ 10 mm in the compression side. Similarly, the column was detailed with 4 Φ 10 longitudinal rebars and 4 Φ 8 mm stirrups. Figure 4 shows rebar detailing of Part-II specimen.

2.3.2. Material Properties of Part-II Specimen. RC flat slab Part-II specimen was reinforced with 10 mm diameter deformed rebars, whereas column stirrups were made of 8 mm diameter plain rebars. The deformed and plain bars had yield stresses of 410 and 270 MPa, respectively. The flat slab had concrete compressive strength of 25 MPa. Table 3 shows details of flat slab concrete and rebar material properties.

2.4. Finite Element Modeling of Part-II Specimen Using ANSYS Software Program. A sequential coupled-field analysis was performed to simulate fire loading using ANSYS software program. First, heat transfer thermal analysis is performed followed by coupled structural analysis. Briefly, temperatures at each node of a FE model are evaluated from thermal analysis and used as input data in following structural analysis. Finally, structural evaluations are performed to determine the structural collapse that occurs when a structure is exposed to both fire and applied forces [16].

2.4.1. Fire Loading. In the present study, applied fire loading was characterized using fire loading curve from the international standardization organization (ISO834) [17]. The fire loading curve (Figure 5) is characterized using the following equation:

$$T = 345 \log (8t + 1) + 20, \quad (1)$$

where T indicates temperature, in degrees celsius, and t indicates time, in minutes.

2.4.2. Sequential Coupled-Field Finite Element Analysis. Heat transfer is a measure of thermal load which simulates fire loading. The amount of heat transferred through a body is referred to as heat transfer. When temperatures of two systems differ, heat is transferred from a higher temperature to a lower temperature, eventually forming the two systems back into equilibrium through conduction, convection, or radiation mechanism [18].

Transient thermal analysis where material properties change over time as a function of temperature was executed to simulate fire loading. Transient thermal analysis requires inputs such as density, thermal conductivity, and specific heat of a material. Aforementioned material inputs were entered as a function of temperature using reduction factors from [19].

In multiphysics simulations, ANSYS software program performs finite element numerical analysis of reinforced concrete slabs subjected to fire in two steps: first, transient thermal analysis is performed, followed by coupled structural analysis [12, 20].

Element types, SOLID70 and SURF152, from ANSYS element library were used to model concrete and target fire loading surface area in transient thermal FE analyses, respectively. Eurocode [19] was used to define the thermal material properties of concrete. Applying sequential coupled-field analysis technique requires first transient thermal analysis to be completed, and this is followed up performing structural analysis using nodal temperature results from former analysis as an input to latter FE structural analysis [12, 21]. However, FE model and geometry must remain the same in both analysis types.

Perfect bond was assumed between concrete and GFRP rebars. This assumption implies that GFRP rebar nodes in a FE model have identical nodal temperature value with parent concrete element.

In sequential coupled-field analysis, four procedures need to be executed while moving from thermal analysis to coupled structural analysis. First, thermal element types are switched with equivalent structural elements. In this study, thermal element SOLID70 was swapped with SOLID185 and CPT 215 structural elements [12]. Second, concrete and steel rebar mechanical are input as a function of temperature. In the present article, reduction factors from Eurocode [19] were employed to define concrete and steel rebar material properties as a function of temperature. Third, SURF152 elements are deleted from the FE model. SURF152 element was used to define target fire exposed external flat slab concrete surfaces in thermal analysis, and they are no longer required in a follow up coupled structural analysis.

Finally, in fourth step, boundary conditions and structural load are applied before performing coupled structural FEA. In this study, boundary conditions were applied at plane of symmetry ($U_X = 0$) and support locations (U_x, U_y, and $U_z = 0$) to constrain respective nodal translation degrees of freedom. Next, structural lateral and axial loads were applied, and coupled structural analysis was performed to learn the punching shear behavior of GFRP-reinforcedslab-column connection subjected to post-earthquake fire loading.

2.4.3. Geometry, Boundary Conditions, and Loading. Taking advantage of symmetry, a half-full model according to experimental details [11] was developed using ANSYS mechanical APDL software program. The model was sectioned along the longitudinal section of a full interior flat slab. This reduces computational and disk storage demands. Simply support boundary condition was applied at flab slab bottom similar to experimental setup [11], and at a plane of symmetry along x-axis, the translation degree of freedom (DOF) in X-direction (U_x) is set to zero (Figure 6).

Thermal loading was applied on $1000 \text{ mm} \times 1000 \text{ mm}$ area of the bottom of a flat slab. This area does not include support consistent with the experimental setup. The initial reference temperature was set to 20°C and then ISO-834 fire curve was gradually applied for 1-hour on flat slabs tension surface to simulate thermal loading. A displacement-controlled loading of 10 mm vertical displacement was applied at the top of a column to simulate gravity loading.

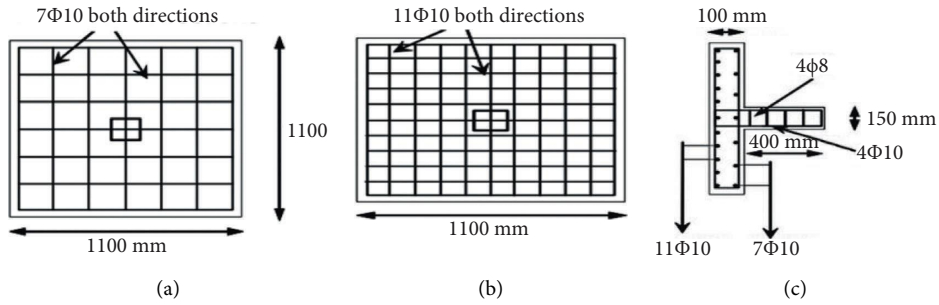

Figure 4: Reinforcement detailing of part-II specimen [11]. (a) Compression reinforcement. (b) Tension reinforcement. (c) Center line section.

Table 3: Material properties of concrete and reinforcement [11].

Materials				
Concrete	Compressive strength, fc (MPa)			
	25			
Reinforcement	Bar size	Bar diam. (mm)	Elastic tensile modulus (GPa)	Yield strength in (MPa)
Steel main bar	Φ10	10	200	410
Steel stirrup	Φ8	8	200	270

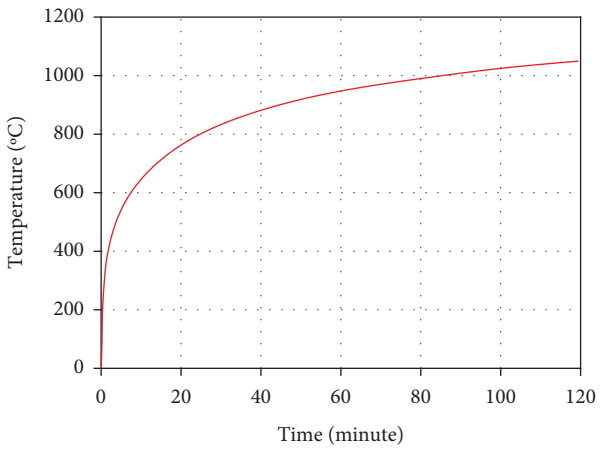

Figure 5: ISO-834 fire curve [17].

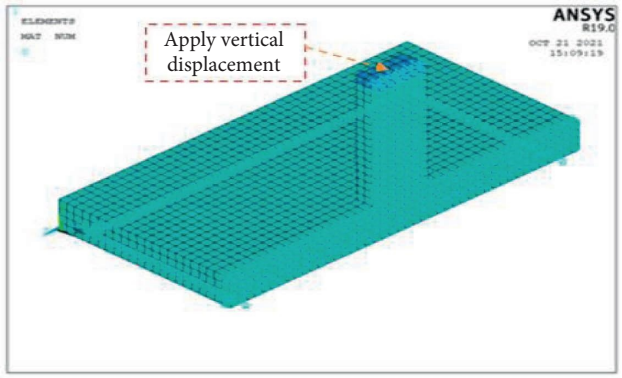

Figure 6: Geometry, meshing, loading, and boundary conditions of part-II specimen.

2.5. Finite Element Parametric Studies on Punching Shear Behavior of GFRP-ReinforcedSlab-Column Connection under Post-Earthquake Fire Loading. This section presents details of proposed finite element models and parameters to investigate punching shear of the GFRP-reinforcedslab-column connection subjected to post-earthquake fire. The parameters considered in the current study are effect of fire exposure duration, concrete grade, slab thickness, fire exposed surface, and column aspect ratio.

Concrete mechanical properties such as compressive strength, tensile strength, and elastic modulus values were multiplied with reduction factors from Eurocode [19] to account for their degradation as a function of temperature. Similarly, reduction factors from Eurocode [19] were used to account for material strength loss as a function of temperature for yield strength and modulus of elasticity of the mechanical material properties of steel rebars. Moreover, ultimate strength and elastic modulus reduction factors of GFRP-reinforced bars were reproduced in [22], and the coefficient of thermal expansion material properties of GFRP bars is adopted from ACI 440.1R-15 [23]. Figures 7–19 present concrete and steel material characterizations at elevated temperatures.

A validated finite element model of the Part-I specimen was used for investigating the proposed parameters. However, additional thermal loading was applied to the bottom surface of flat slab to simulate post-earthquake fire loading. This thermal loading was applied to an area of 950 mm × 1900 mm, excluding support boundary conditions. Table 4 presents a parametric study matrix table showing combination of variables and FEA runs to study the punching shear of the GFRP-reinforcedslab-column connection subjected to post-earthquake fire.

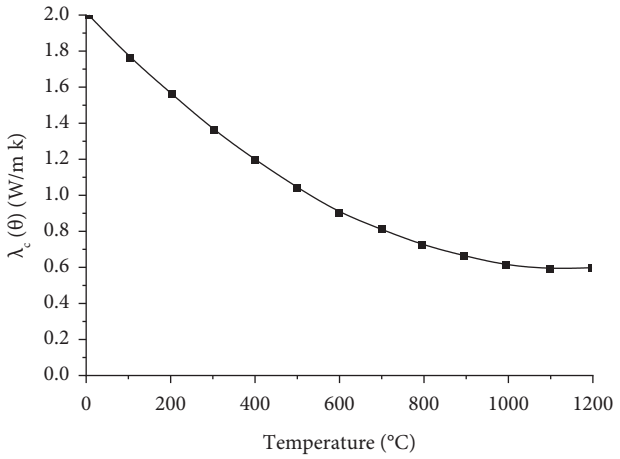

Figure 7: Concrete thermal conductivity [19].

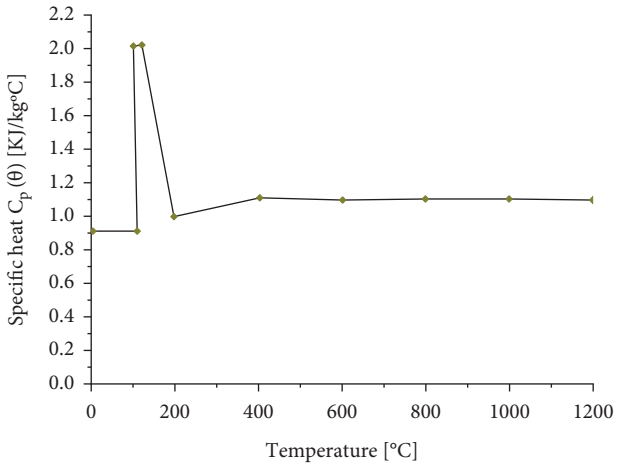

Figure 8: Concrete specific heat variation with temperature [19].

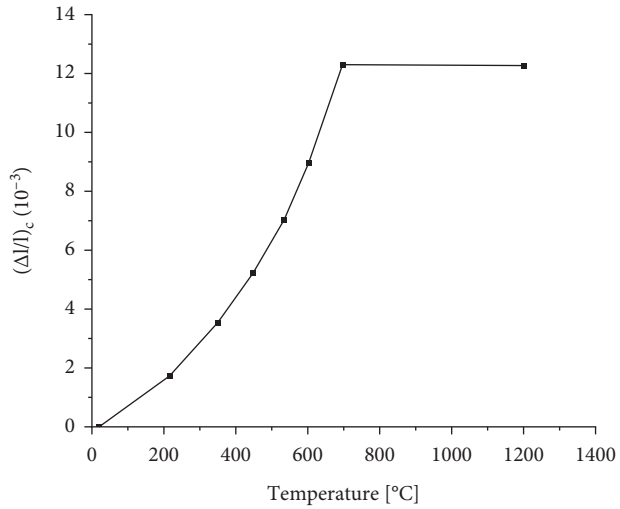

Figure 9: Coefficient of thermal expansion [19].

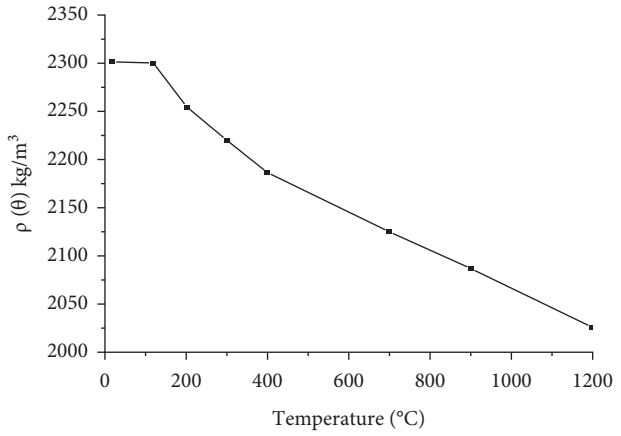

Figure 10: Concrete density variation with temperature [19].

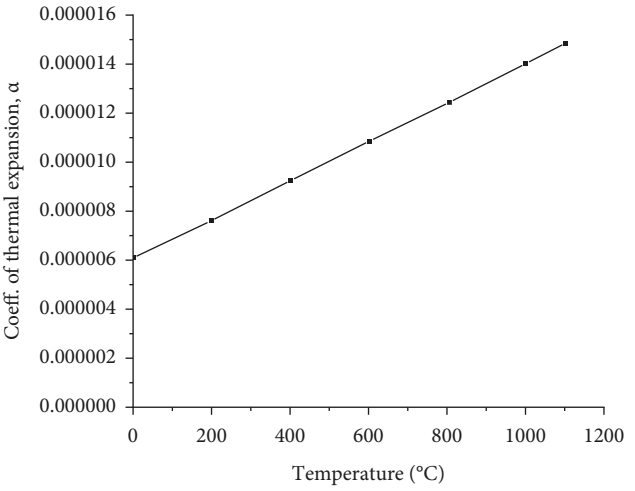

Figure 11: Concrete secant thermal expansion coefficient variation with temperatures [19].

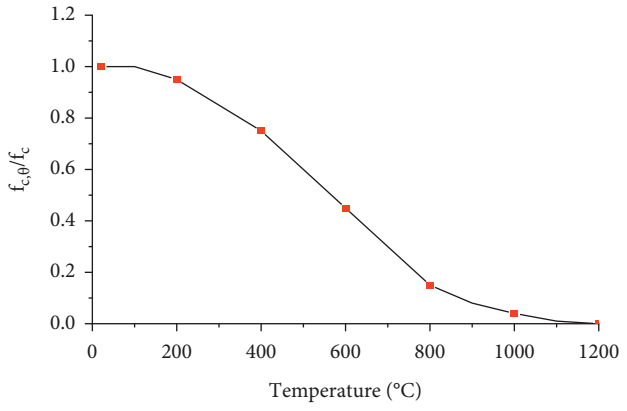

Figure 12: Concrete compressive strength reduction factor at elevated temperatures [19].

2.6. Mesh Sensitivity Study. Employed element types, their mesh size, and aspect ratio affect the accuracy of finite element numerical simulation [25]. A finer mesh typically results in a more accurate solution; however, as high mesh density is used, computation time and disk storage increase exponentially [26]. Therefore, there is a need to choose a reasonable mesh size resulting in convergence of a solution

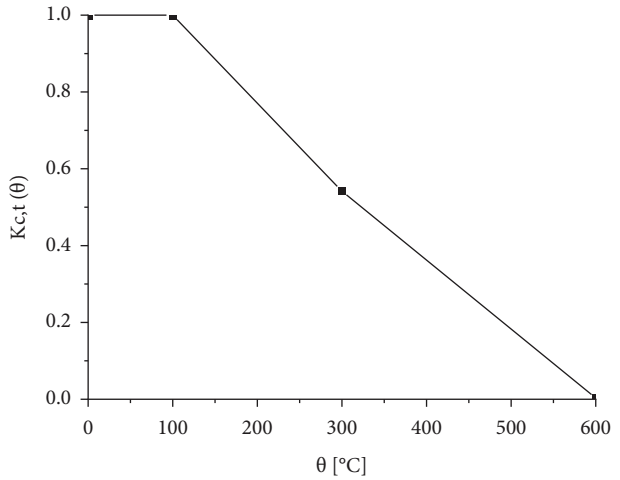

Figure 13: Tensile strength reduction factor at elevated temperatures [19].

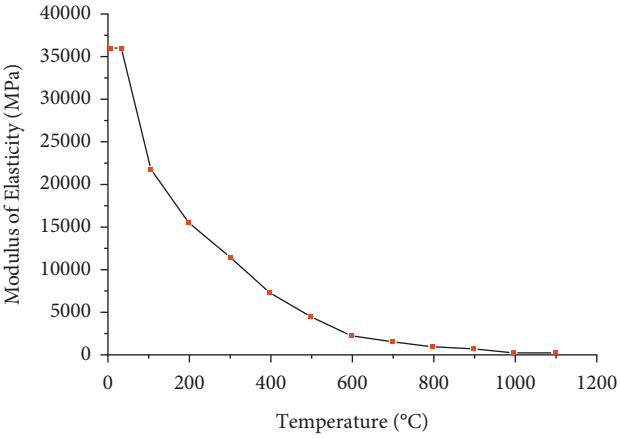

Figure 14: Concrete modulus of elasticity variation with temperature [19].

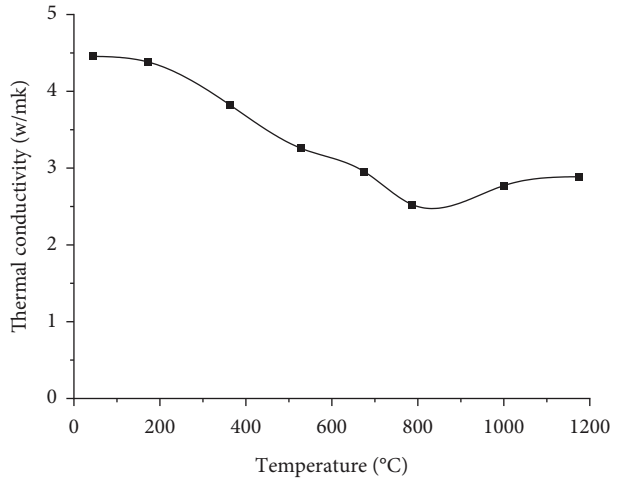

Figure 15: Thermal conductivity of steel at elevated temperatures [24].

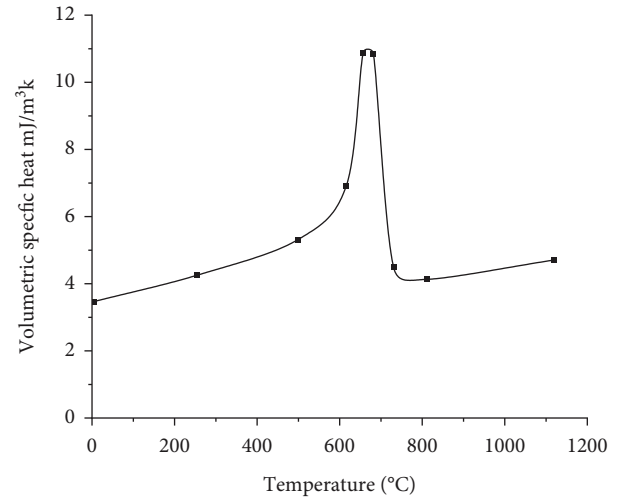

Figure 16: Volumetric specific heat for steel at elevated temperatures [24].

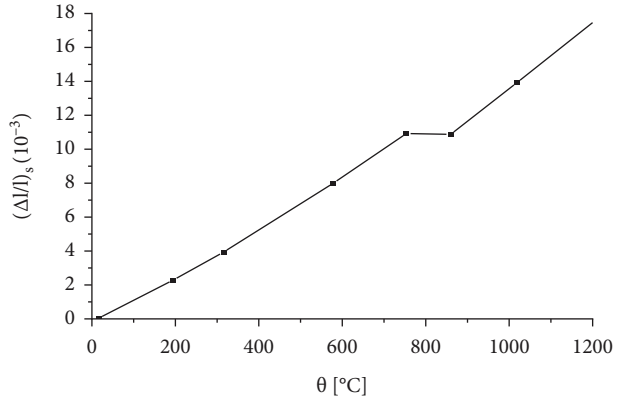

Figure 17: Thermal elongation of steel at elevated temperature [19].

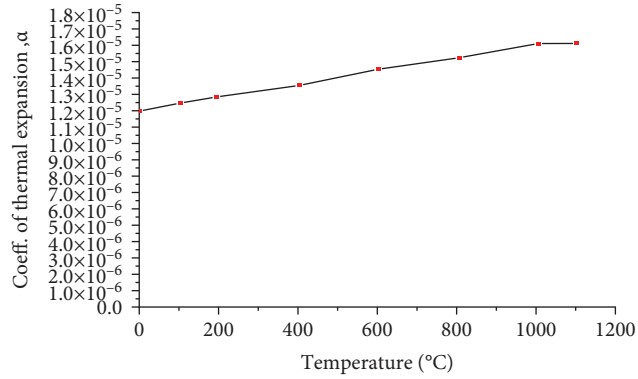

Figure 18: Variation of secant thermal expansion coefficient with temperature [19].

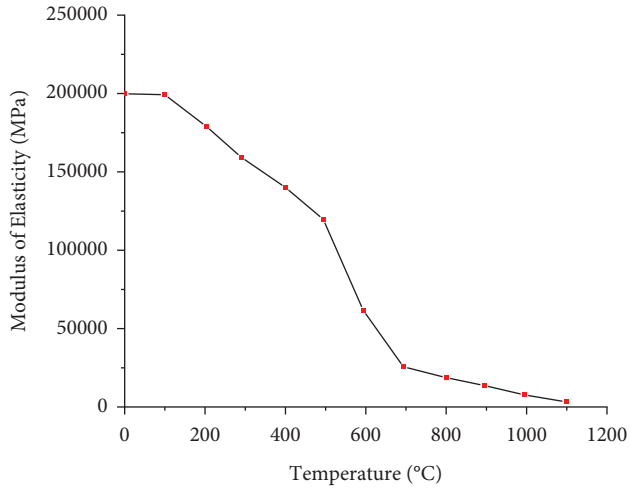

Figure 19: Variation of modulus of elasticity of reinforcement with temperature [19].

Table 4: Parametric study matrix table of GFRP-reinforced slab-column connection with shear reinforcement under post-earthquake fire.

FE model ID	Slab thickens (mm)	Concrete grade (Mpa)	Column aspect ratio (β)	Fire exposure surface	Duration of fire (minute)
Effect of fire duration					
200-45-1-ALL Bs-40	200	45	1	All bottom surface	40
200-45-1- ALL Bs-30	200	45	1	All bottom surface	30
200-45-1- ALL Bs-20	200	45	1	All bottom surface	20
200-45-1- ALL Bs-10	200	45	1	All bottom surface	10
Effect of compressive strength of concrete					
200-35-1- ALL Bs-40	200	35	1	All bottom surface	40
200-30-1- ALL Bs-40	200	30	1	All bottom surface	40
200-25-1- ALL Bs-40	200	25	1	All bottom surface	40
Effect of slab thickens					
150-45-1- ALL Bs-40	150	45	1	All bottom surface	40
175-45-1- ALL Bs-40	175	45	1	All bottom surface	40
250-45-1- ALL Bs-40	250	45	1	All bottom surface	40
Effect of fire exposure side					
200-45-1- ALL Ts-40	200	45	1	All top surface	40
200-45-1-Half Bs-40	200	45	1	Half bottom surface	40
200-45-1-Half Ts-40	200	45	1	Half top surface	40
Effect of aspect ratio					
200-45-1.16- ALL Bs-40	200	45	1.16	All bottom surface	40
200-45-1.33- ALL Bs-40	200	45	1.33	All bottom surface	40
200-45-1.66- ALL Bs-40	200	45	1.66	All bottom surface	40

by performing a mesh sensitivity study. In this study, the aspect ratio of brick element types was set to1, and FE mesh sensitivity study was executed with various element sizes ranging from 25 mm to 50 mm.

Figure 20 presents a comparison of experimental and FEA load deflection result plots for various mesh sizes. Mesh sensitivity FEA results showed a good agreement with experimental results both for Part-I and Part-II specimens. Optimizing FEA accuracy as compared to experimental results, total run time to complete analysis, and disk space usage, a mesh size of 50 mm and 25 mm was selected for subsequent FE parametric studies on Part-I and Part-II specimens.

3. Results and Discussion

This section describes the findings of validated and parametric FEA results. The main parameters investigated in this study include effects of post-earthquake fire exposure duration, concrete grade, slab thickness, fire exposed surface, and column aspect ratio on punching performance of GFRP-reinforcedslab-column connections. Moreover,

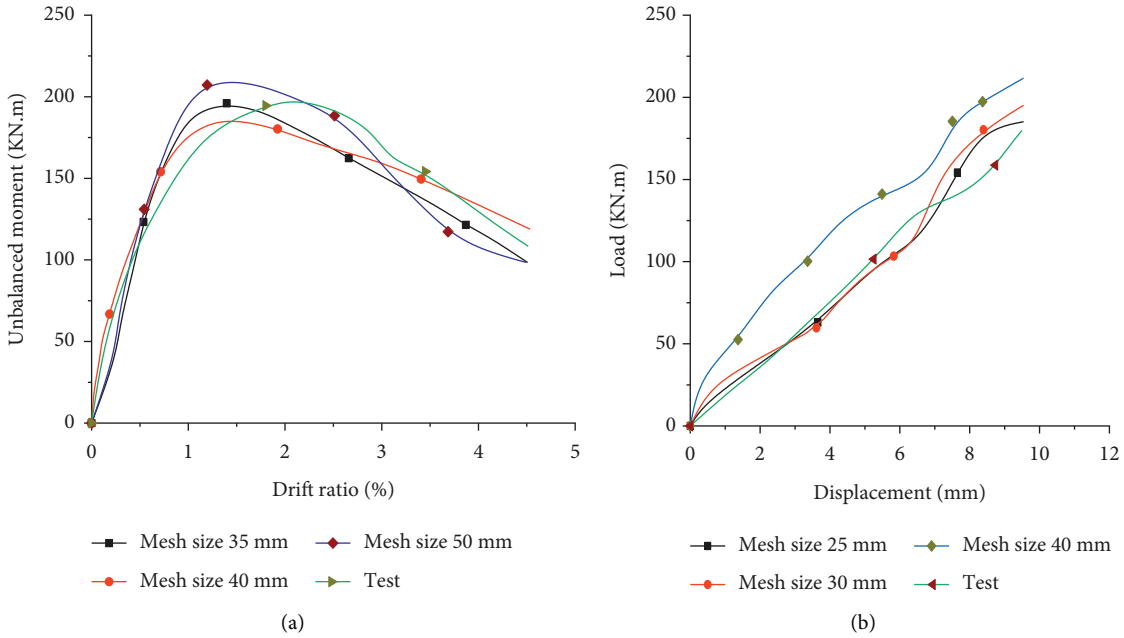

Figure 20: Mesh sensitivity study. (a) Effect of different mesh size for Part-I specimen. (b) Effect of different mesh size for Part-II specimen.

comparisons of FE validation analysis results and two experimental tests of two interior slab-column connections [3, 11] are presented.

3.1. FE Validation Analysis Results. Finite element studies and their comparison with the experimental test results for verification are extremely important in order to idealize the real behavior of the tested specimens and predict the behavior of other specimens that cannot be tested experimentally. This verification could provide evidence about the applicability of the finite element model to investigate structural behavior. In this study, two experimental tests from the article [3, 11] on GFRP-reinforcedslab-column connection with GFRP shear reinforcement provided at 2 d from the face of the column were used for FE validation analysis.

The accuracy of the nonlinear finite element model was evaluated by comparing the NLFEA results of these two specimens with the experimental result in terms of unbalanced moment drift ratio and failure pattern for model G6CS–2d tested by [3] and also for model S1 tested by [11], in terms of load-displacement response and failure pattern.

3.1.1. Unbalanced Moment Drift Ratio for G6CS-2d Specimen and Load-Displacement for S1 Specimen Response

(1) GFRP-ReinforcedSlab-Column Connection Specimen, G6CS-2d. Figure 21 shows comparison of the unbalanced moment drift ratio response obtained from NLFEA compared with the experimental results of the specimen G6CS-2d.

The NLFEA's unbalanced moment drift ratio response of the specimen GFRP-reinforcedslab-column connection (G6CS-2d) is a good agreement with the experimental result. The maximum unbalanced moment obtained from the

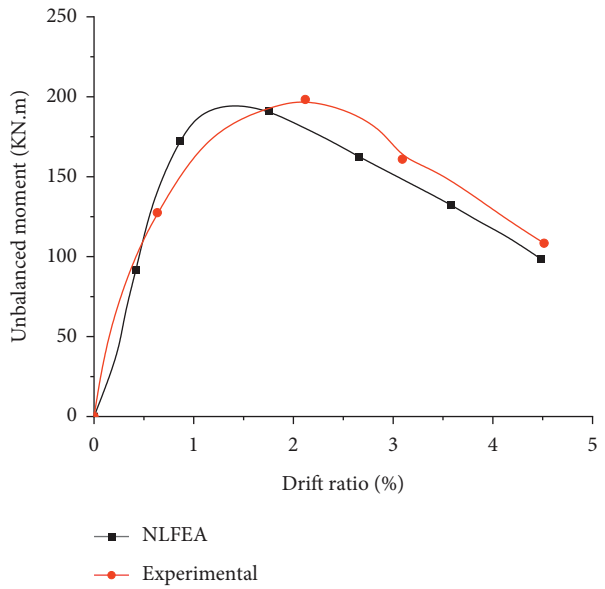

Figure 21: Unbalanced moment drift ratio graph for G6CS-2d specimen.

NLFEA of this specimen is 1.32% lower than the maximum unbalanced moment reported from the experimental study (see Table 5). The higher stiffness observed in NLFEA results as compared to the experimental results might be due to the formation of microcracks in the experimental test, thus reducing its stiffness, whereas in finite element models do not fully capture the development of these microcracks [27]. Also, the perfect bond assumption between concrete and reinforcement in developed finite element models might account for the aforementioned minor differences between NLFEA and experimental results.

Table 5: Maximum unbalanced moment and maximum load comparisons of NLFEA prediction with the test results of the two specimens.

Specimen	Maximum lateral load (kN)		Maximum unbalanced moment (KN.m)			
Specimen 1 ID name	NLFEA	Test	Error (%)	NLFEA	Test	Error (%)
G6CS–2d	148.68	150.9	−1.47	195.985	198.6	−1.32
Specimen	Maximum axial load (KN)		Prediction			
Specimen 2 ID name	NLFEA	Test	Error (%)			
S1	185.21	179	3.47			

(2) Reinforced Concrete Flat Slab Specimen, S1. As can be seen in Figure 22, the load-displacement curves of NLFEA and experimental results showed good agreement. The maximum load obtained from NLFEA analysis was 3.47% higher than the maximum load reported from the experimental study (see Table 5). Table 5 shows accuracy of NLFEA results for the two specimens as compared with the experimental test results. It describes the overall model accuracy of the NLFEA. The error (%) was evaluated based on the relation given in [28] and as shown in the following:

$$\text{error}(\%) = \left(\frac{\text{NLFEA} - \text{test result}}{\text{test result}}\right) * 100. \quad (2)$$

In all cases, the FEA results of the connection punching shear cracking, unbalanced moment, and maximum load fall to an error of less than 5% implying that the finite element response of the specimens is in good agreement with experimental test results. This indicates that employed material properties and constitutive models were capable of capturing the response of GFRP-reinforcedslab-column connection with GFRP shear reinforcement.

3.1.2. Failure Patternsald

(1) GFRP-ReinforcedSlab-Column Connection Specimen, G6CS-2d. Figure 23 shows side by side comparison of crack patterns of NLFEA and experimental test results at failure load for specimens G6CS-2d.

Figure 23 shows that the numerical model shows good agreement between the punching shear cracking pattern obtained from NLFEA and the punching shear crack propagation pattern reported in the experimental study. In both results, punching cracking patterns concentrated on GFRP-reinforcedslab-column connection.

(2) Reinforced Concrete Flat Slab Specimen, S1. Figure 24 presents FEA temperature distributions of flat slab specimen, S1 after 3600sec fire exposure, whereas Figure 25 shows the comparison of crack patterns in specimens S1 between NLFEA and experimental test results at the failure load stage.

Overall failure patterns as predicted by NLFEA showed good agreement with experimental test results. Therefore, developed FE models can be used as an effective and reliable tool to study effect of various influential parameters on post-earthquake fire punching shear behavior of GFRP-reinforcedslab-column connections.

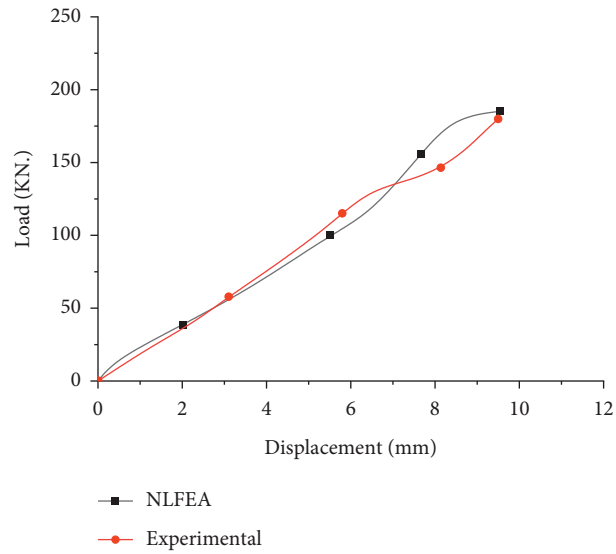

Figure 22: Load-displacement curve for specimen S1.

Aforementioned validated FE model was used as a controlling specimen of GFRP-reinforcedslab-column connection with GFRP shear reinforcement provided at 2d from the face of the column under an earthquake and axial load at ambient temperature. Then, in subsequent parametric studies, the validated FE model was subjected to post-earthquake fire at the bottom surface of the slab besides to lateral load and 0%, 10%, 20%, and 50% axial loading levels. Nevertheless, except for the aforementioned applied loads, the control specimen's detailing had been kept identical to the experimental test in [3]. FEA results such as unbalanced moment drift ratio and drift ratio-fire duration response for an all-varied axial load level loading are discussed below.

Figures 26–29 show the effect of varied axial load levels on the unbalanced moment drift ratio and drift ratio-fire duration response. FEA results showed that changes in axial loading levels affected slab-column connection fire resistance performance. As the axial load ratio increased from 0% to 10% to 20% and 50%, slab-column connection fire resistance reduced to 49.87 min, 25.48 min, 5.48 min, and 4.65 min, respectively. For subsequent parametric studies, a FE model with 0% axial load level, 3.07% drift ratio, and 40 min post-earthquake fire exposure duration was used as a control specimen. Next, Figures 30–33 present nodal temperature distribution, unbalanced moment drift ratio, homogenized concrete damage, and rebar strain for a 0% axial load level control specimen.

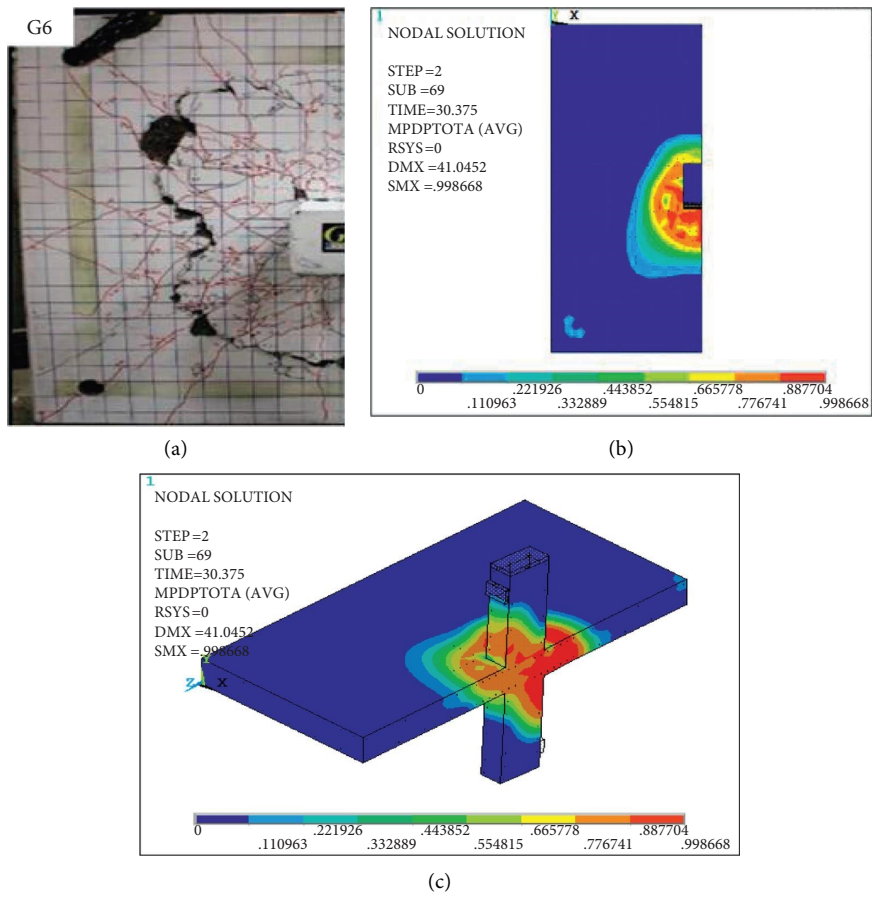

Figure 23: Comparison of concrete damage of specimen G6CS-2d at failure load. (a) Experimental half-scale [8]. (b) FEA half-scale plan view. (c) FEA half-scale 3D view.

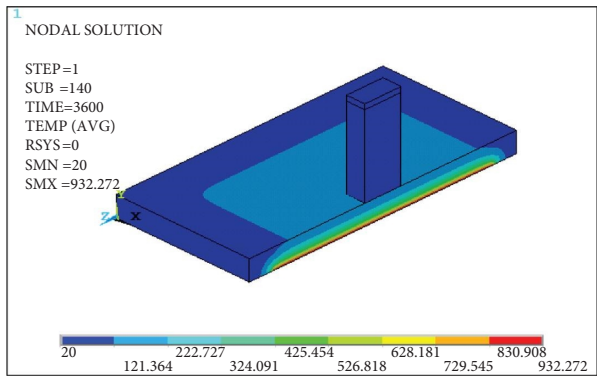

Figure 24: FEA temperature distributions after 3600 sec fire exposure at the bottom of specimen S1 slab.

3.2. FEA Parametric Studies on GFRP-ReinforcedSlab-Column Connections with GFRP Shear Reinforcement Subjected to Post-Earthquake Fire. This section presents the response of GFRP-reinforcedslab-column connections with GFRP shear reinforcement provided at 2d from the face of the column under post-earthquake fire loading. Effects of influential parameters such as fire exposure duration, concrete grade, slab thickness, fire exposed surface, and column aspect ratio are investigated thoroughly.

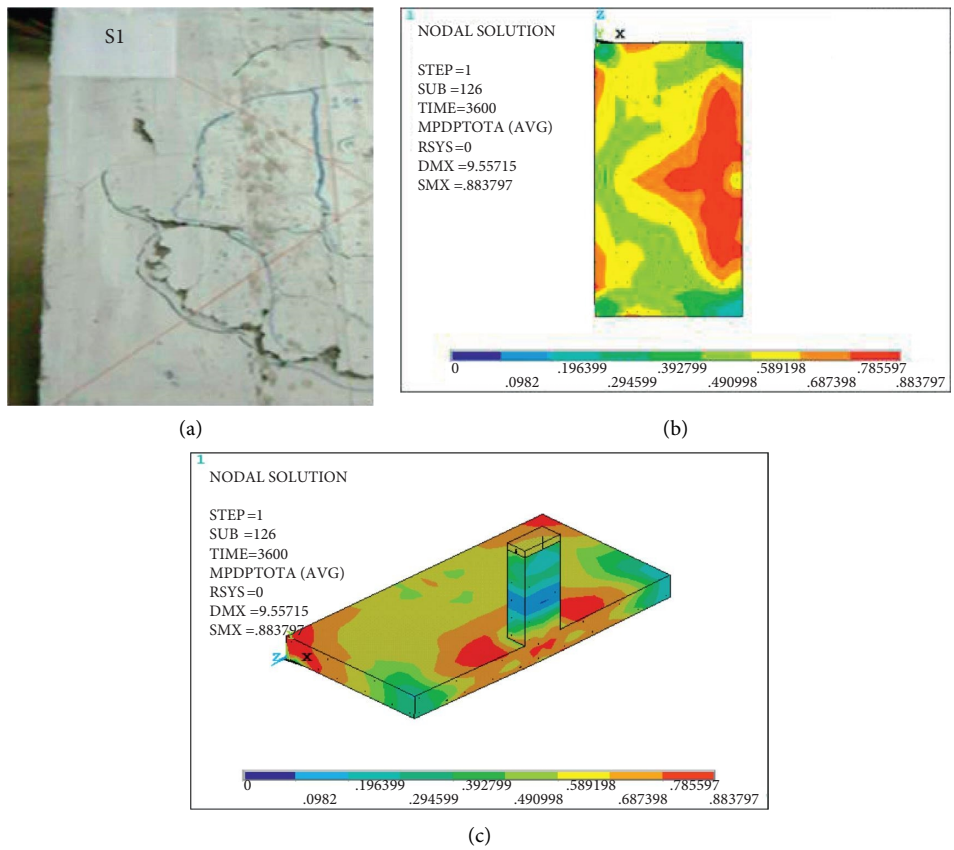

Figure 25: Comparison of concrete damage of specimen S1 due to 3600 sec fire exposure and maximum load. (a) Experimental half-scale [11]. (b) FEA half-scale plan view. (c) FEA half-scale 3D view.

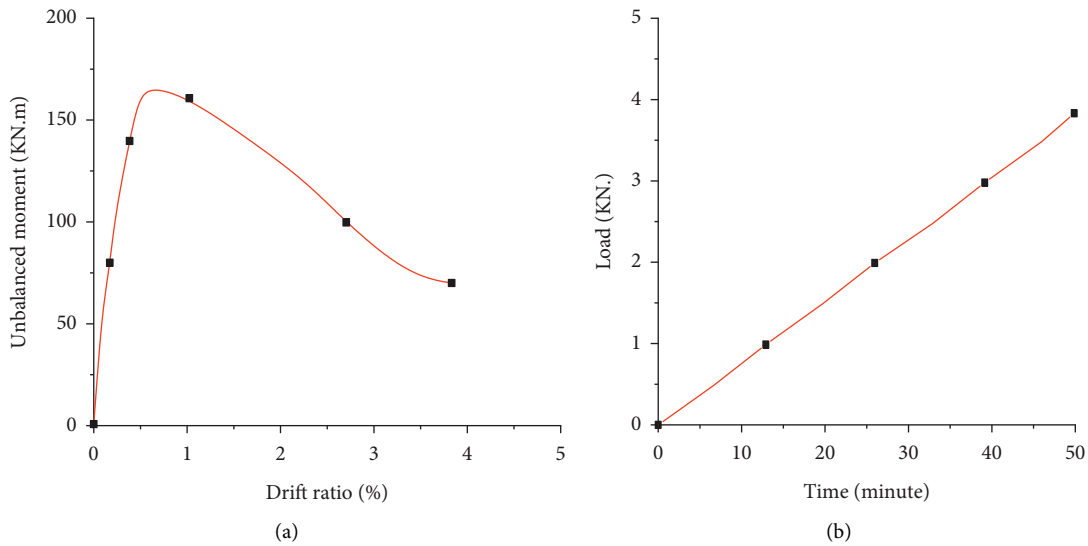

Figure 26: (a) Unbalanced moment drift ratio response and (b) drift ratio-fire exposed duration response of 0% axial load level.

3.2.1. Effect of Post-Earthquake Fire Exposure Duration. Three different fire exposure durations of 600, 1200, and 1800 seconds were selected and applied to study the impact of fire exposure duration on GFRP-reinforcedslab-column connections under post-earthquake fire loading. Next, the unbalanced moment drift ratio and concrete damage results of these specimens are examined in contrast to the control specimen.

FEA results of GFRP-reinforcedslab-column connections under post-earthquake fire exposure for

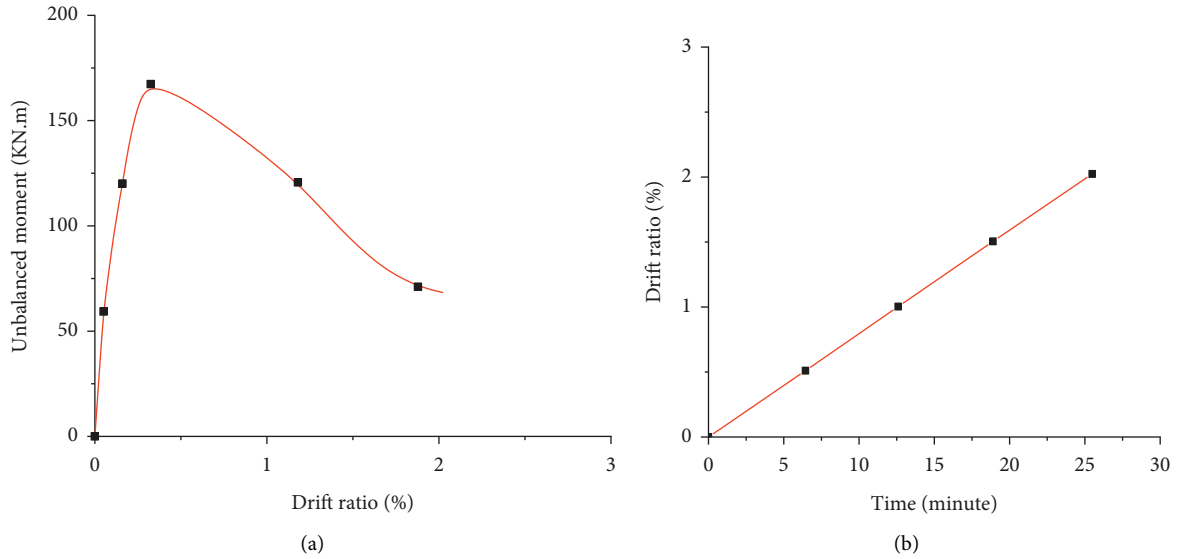

Figure 27: (a) Unbalanced moment drift ratio response and (b) drift ratio-fire exposed duration response of 10% axial load level.

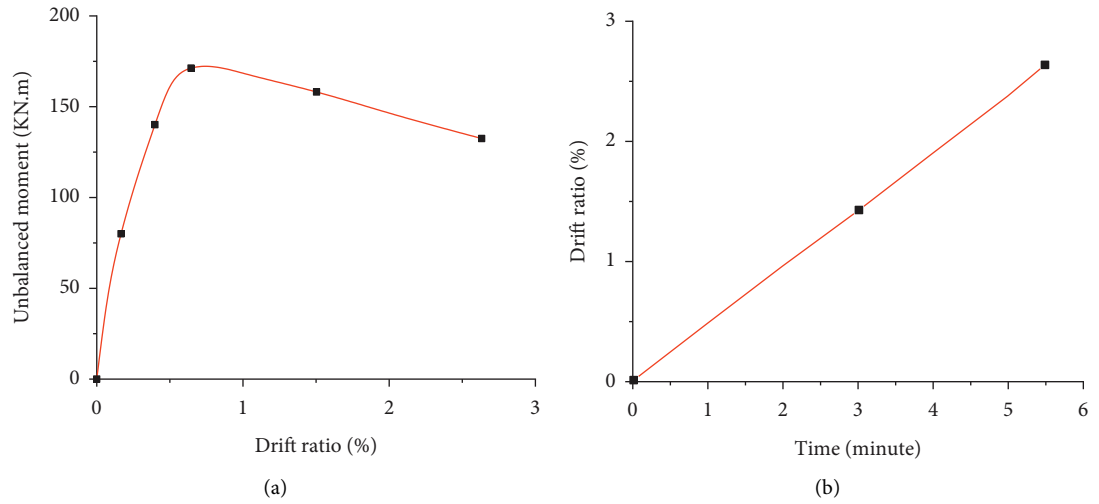

Figure 28: (a) Unbalanced moment drift ratio response and (b) drift ratio-fire exposed duration response of 20% axial load level.

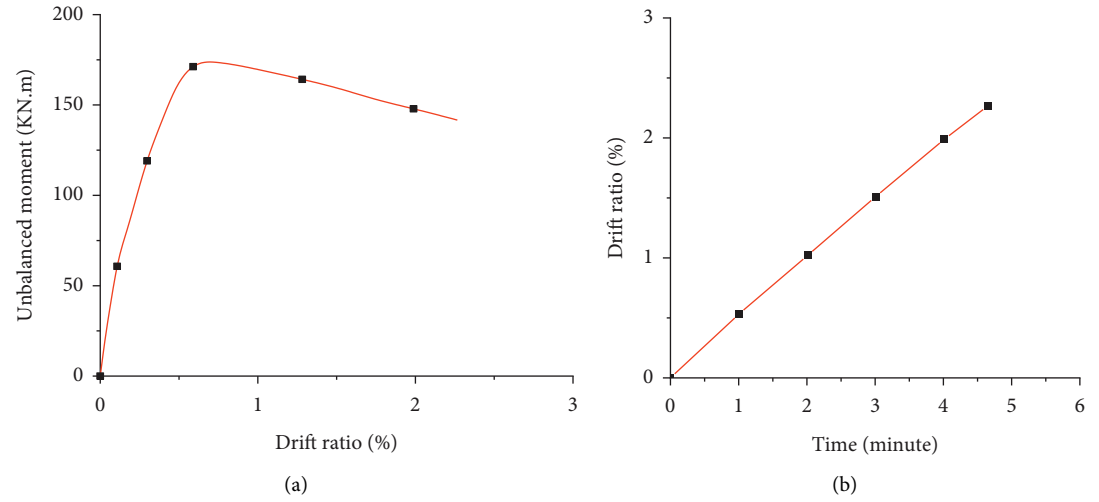

Figure 29: (a) Unbalanced moment drift ratio response and (b) drift ratio-fire exposed duration response of 50% axial load level.

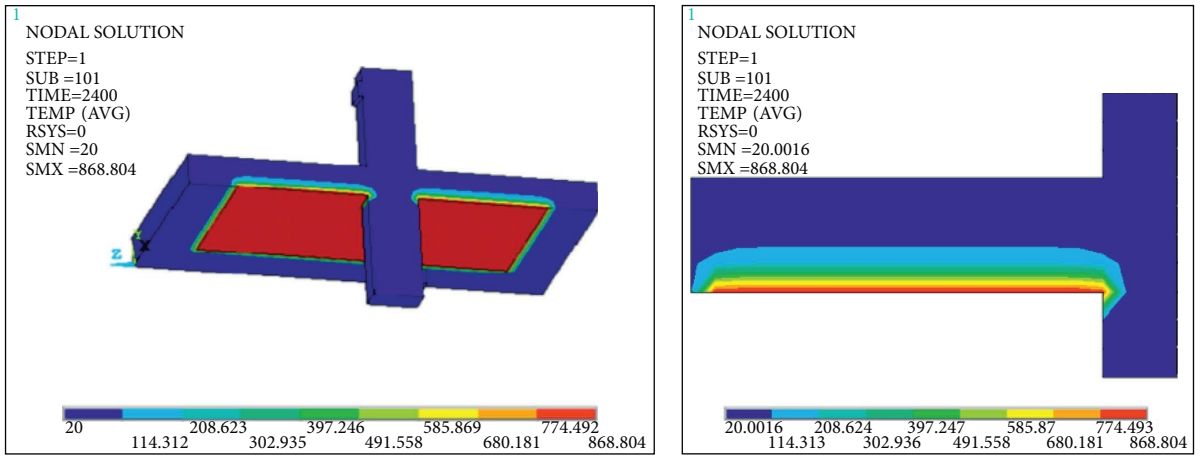

Figure 30: Nodal temperature distribution of control specimen with 2400 sec fire exposure at the bottom surface of slab. (a) 3D view of nodal temperature distribution of the control specimen. (b) Centerline section view of nodal temperature distribution of the control specimen.

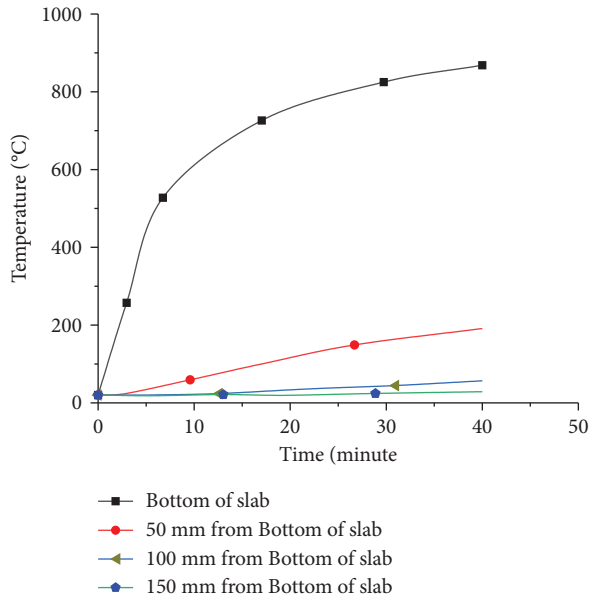

Figure 31: The control specimen's time versus temperature behavior during a 2400 sec fire exposure at the bottom surface of a slab at varying slab depths.

durations of 1800, 1200, and 600 seconds exhibited maximum unbalanced moment of 174.60 KN·m, 179.28 KN·m, and 187.77 KN·m, respectively (Figure 34). A decrease in post-earthquake fire exposure duration from 2400 to 600 seconds resulted in peak of unbalanced moment drift ratio in slab-column connections in ranges of 1.89% to 9.58%. This implies higher post-earthquake fire exposure results in increase in temperature distribution of a specimen leading to deterioration of concrete and reinforcement material properties.

Figure 35 presents the nodal temperature distribution for various post-earthquake fire duration and as post-earthquake fire duration increased, so does concrete damages in respective specimens.

3.2.2. Effect of Concrete Grade. Analytical formulas in ACI and Eurocode codes of practice use compressive strength of concrete as a key parameter to evaluate punching shear stress of concrete slab. The control specimen has C-45 MPa concrete grade, and the current parametric study on grade of concrete three different concrete grades was considered, namely, C-25 MPa, C-30 MPa, and C-35 MPa.

Figure 36 shows that the increasing concrete grade leads to an increase in punching shear capacity. Maximum unbalanced moment of 125.48 KN·m, 138.60 KN·m, and 150.48 KN·m was recorded for GFRP-reinforcedslab-column connections with concrete grades of C-25, C-30, and C-35, respectively, and as compared to control, the losses were −26.77%,−19.11%, and −12.18%. Raising

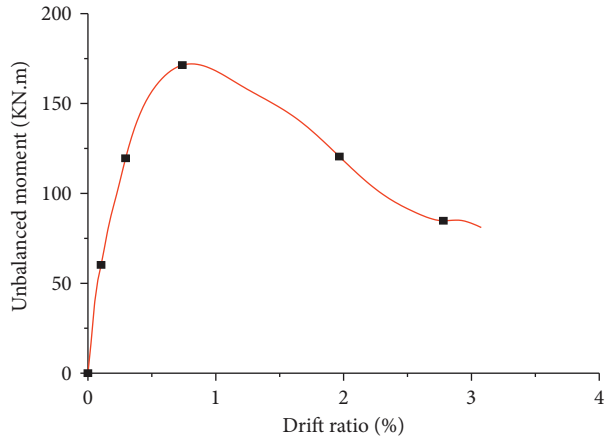

Figure 32: Control specimen's unbalanced moment drift ratio response with 2400 sec fire exposure.

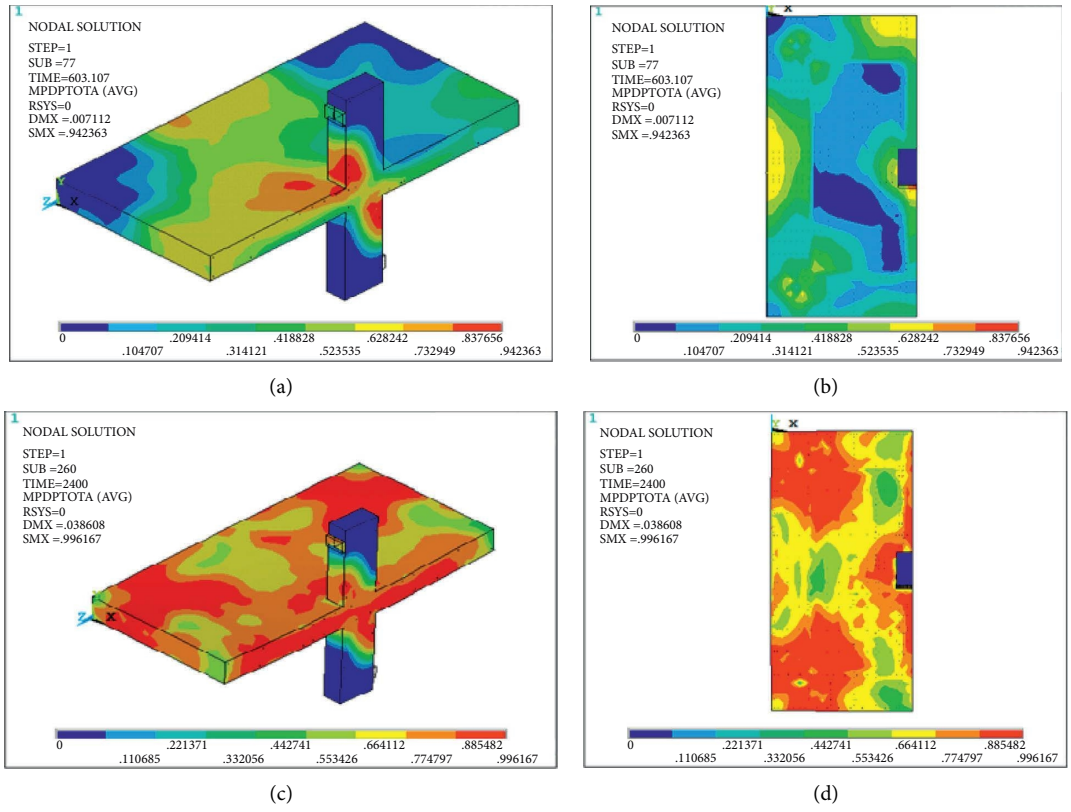

Figure 33: Total concrete damage to control specimen due to 2400 sec fire exposure at the bottom of the slab. (a) Total concrete damage at maximum load. (b) Bottom surface total concrete damage at maximum load. (c) Total concrete damage at failure load. (d) Bottom surface total concrete damage at failure load.

concrete grade has shown better punching shear carrying capacity of GFRP-reinforcedslab-column connections subjected to post-earthquake fire.

Figure 37 shows FEA concrete damage results of GFRP-reinforcedslab-column connections subjected to post-earthquake fire for concrete grades C-25, C-30, and C-35. The results imply that concrete grade has minor effect on lessening concrete damage.

3.2.3. Effect of Slab Thickness. Three different slab thicknesses of 150 mm, 175 mm, and 250 mm were selected to study effect of slab thickness on behavior of GFRP-reinforcedslab-column connections subjected to post-earthquake fire. FEA results showed thickness of the slab affected structural performance of GFRP-reinforcedslab-column connections subjected to post-earthquake fire.

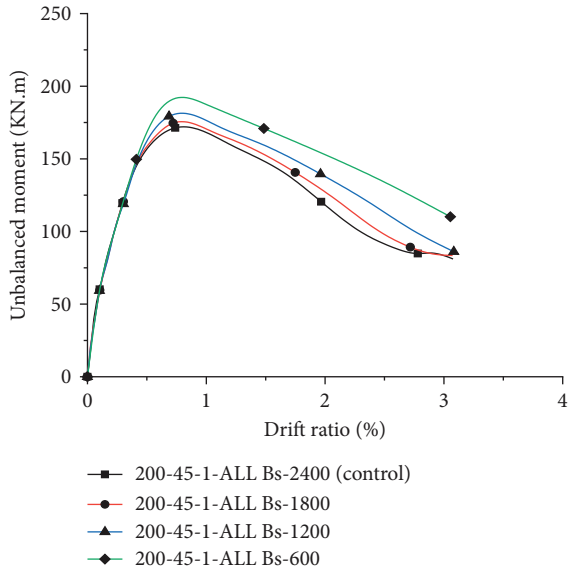

Figure 34: Effect of post-earthquake fire exposure duration on unbalanced moment drift ratio response.

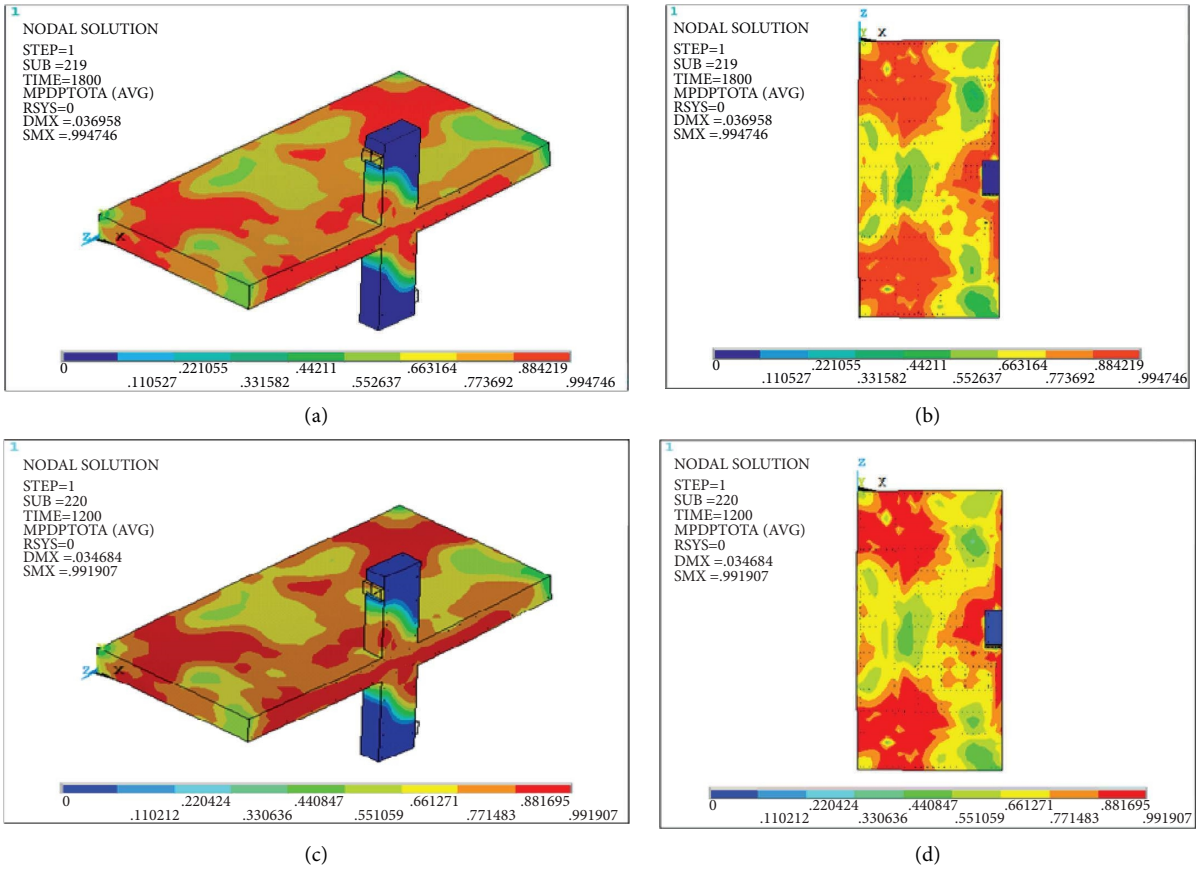

Figure 35: Continued.

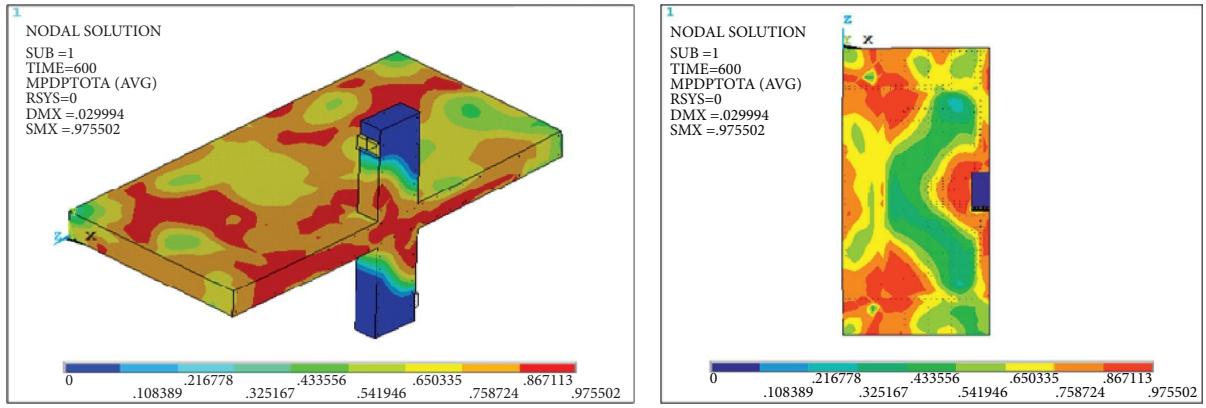

(e) (f)

Figure 35: Concrete damage of specimens with varying post-earthquake fire exposure durations. (a) Specimen 200-45-1-ALL Bs-1800. (b) Bottom surface. (c) Specimen 200-45-1-ALL Bs-1200. (d) Bottom surface. (e) Specimen 200-45-1-ALL Bs-600. (f) Bottom surface.

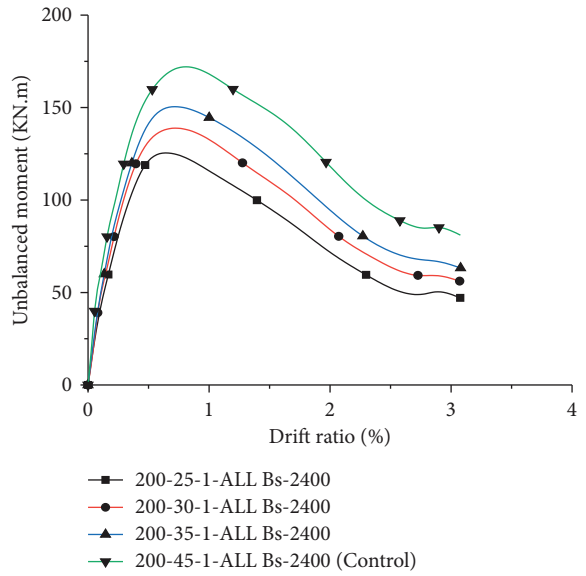

Figure 36: Effect of concrete grade on unbalanced moment drift ratio.

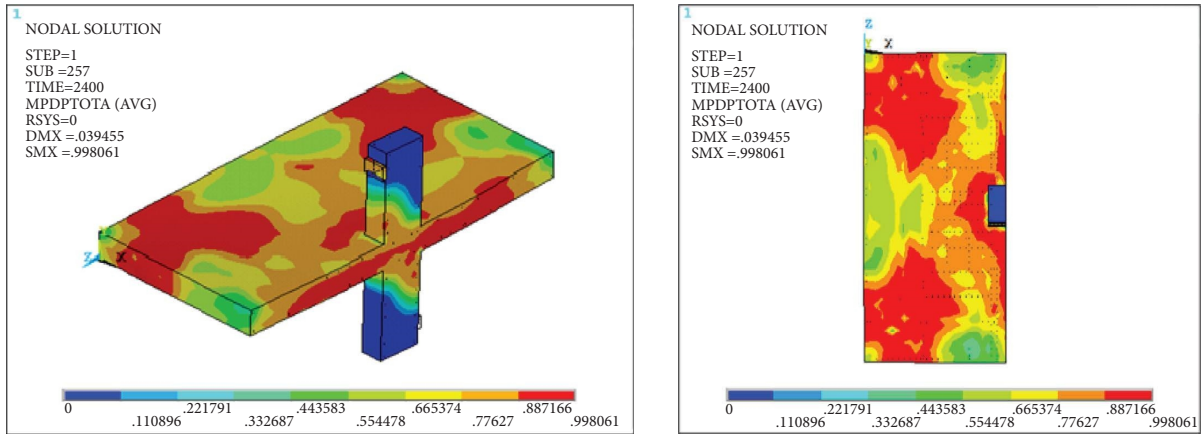

(a) (b)

Figure 37: Continued.

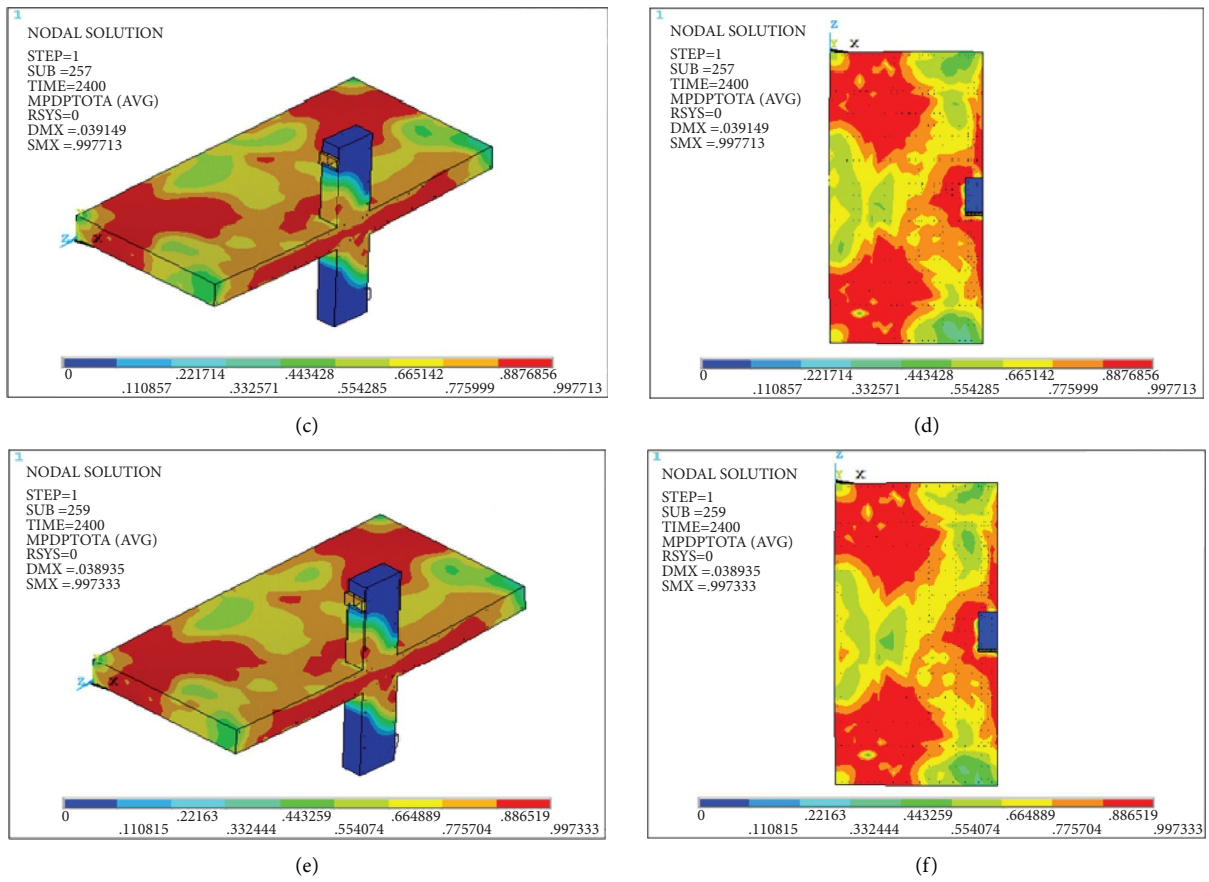

Figure 37: Concrete damage of specimens with varying concrete grade. (a) Specimen 200-25-1-ALL Bs-2400. (b) Bottom surface. (c) Specimen 200-30-1-ALL Bs-2400. (d) Bottom surface. (e) Specimen 200-35-1-ALL Bs-2400. (f) Bottom surface.

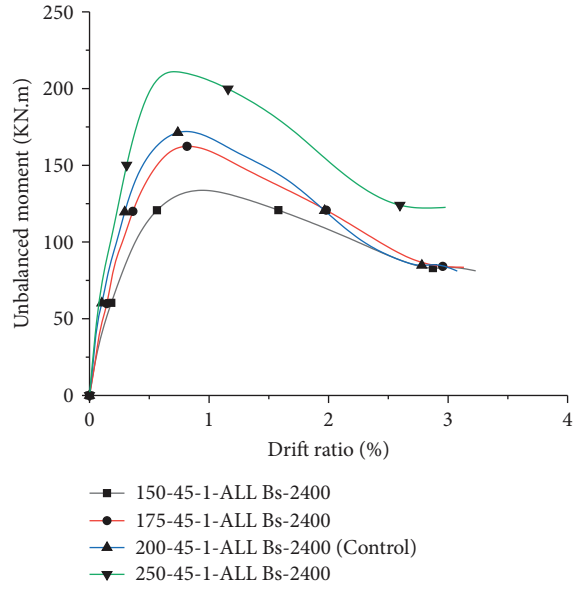

Figure 38: Effect of slab thickens on unbalanced moment drift ratio.

FEA results for slab thicknesses of 150 mm, 175 mm, and 250 mm displayed ultimate moment of 133.24 KN·m, 162.34 KN·m, and 210.50 KN·m (Figure 38), and as compared to control, variations were −22.24%, −5.26%, and 22.85%. Increasing slab thickness decreased heat transfer across slab section resulting minor concrete

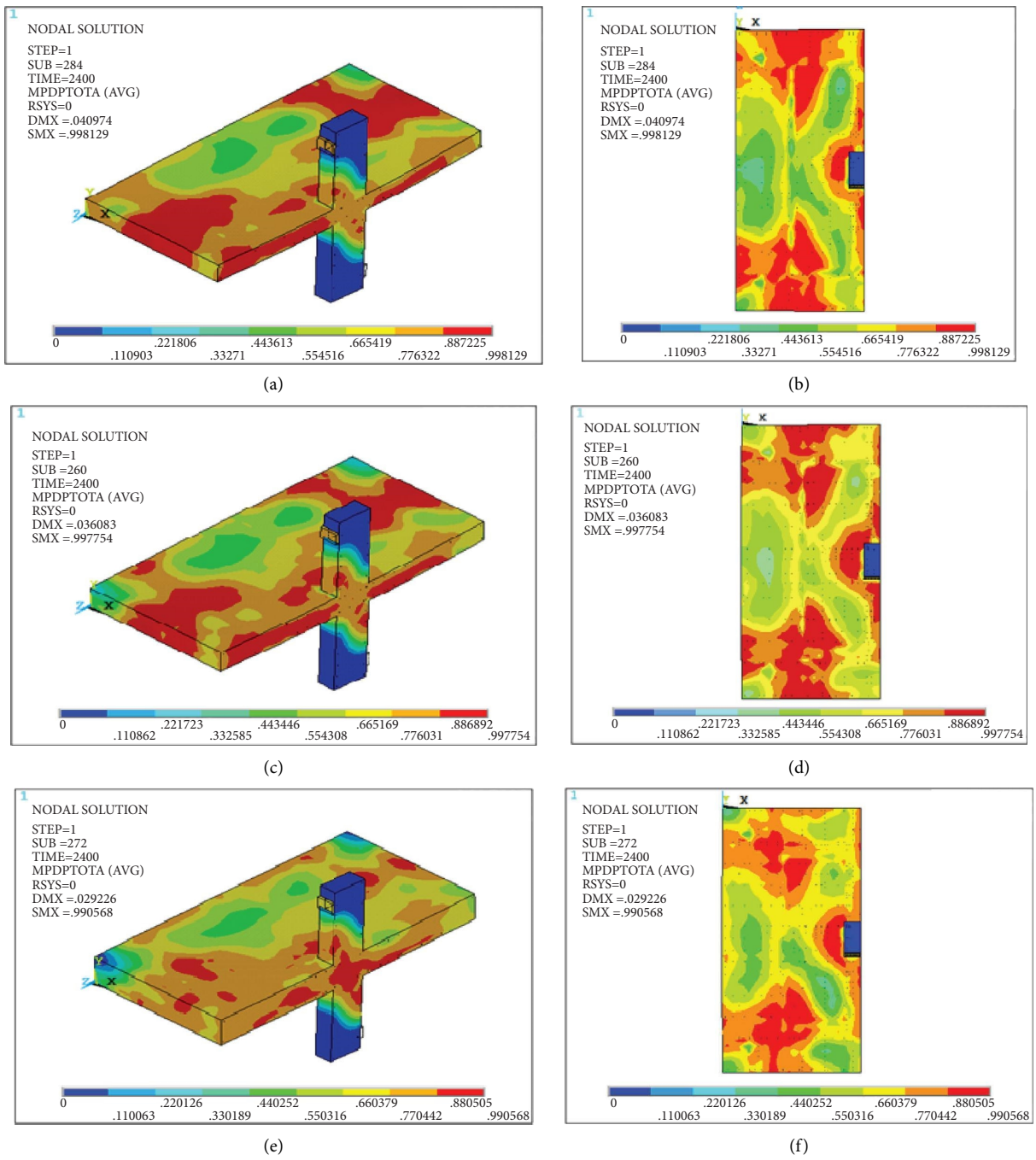

Figure 39: Concrete damage of specimens with varying slab thickness. (a) Specimen 150-45-1-ALL Bs-2400. (b) Bottom surface. (c) Specimen 175-45-1-ALL Bs-2400. (d) Bottom surface. (e) Specimen 250-45-1-ALL Bs-2400. (f) Bottom surface.

deterioration. Moreover, increasing slab thickness enlarged effective depth of the specimens which in turn raised shear resistance of concrete due to aggregate interlocking.

Figure 39 presents the nodal temperature variations for GFRP-reinforcedslab-column connections with slab thicknesses of 150 mm, 175 mm, and 250 mm. As slab thickness increased, the nodal temperature variations across slab thickness were reduced.

3.2.4. Effect of Fire Exposed Surface. Three varied surface areas such as all top slab surface, half top slab surface, and half bottom slab surface were selected, and post-earthquake fire loading was applied on aforementioned proposed exposed surfaces of slab to study impact of exposed surface on post-earthquake fire behavior of GFRP-reinforcedslab-column connection.

FEA results indicated that as compared to control, maximum unbalanced moment peaked by 7.73%, 14.18%,

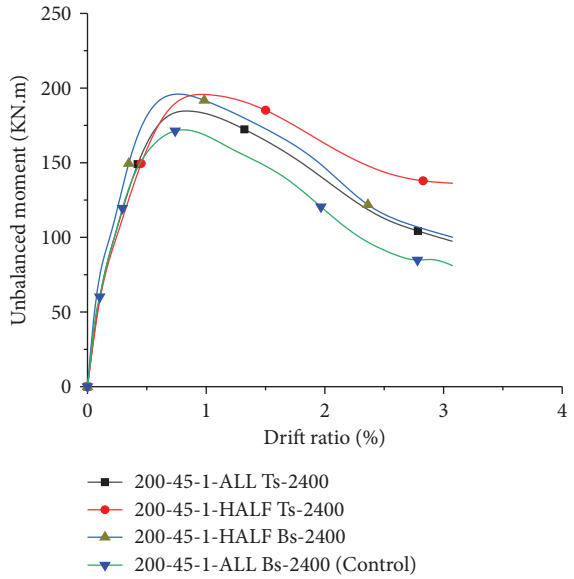

Figure 40: Effect of post-earthquake fire exposed surfaces on unbalanced moment drift ratio.

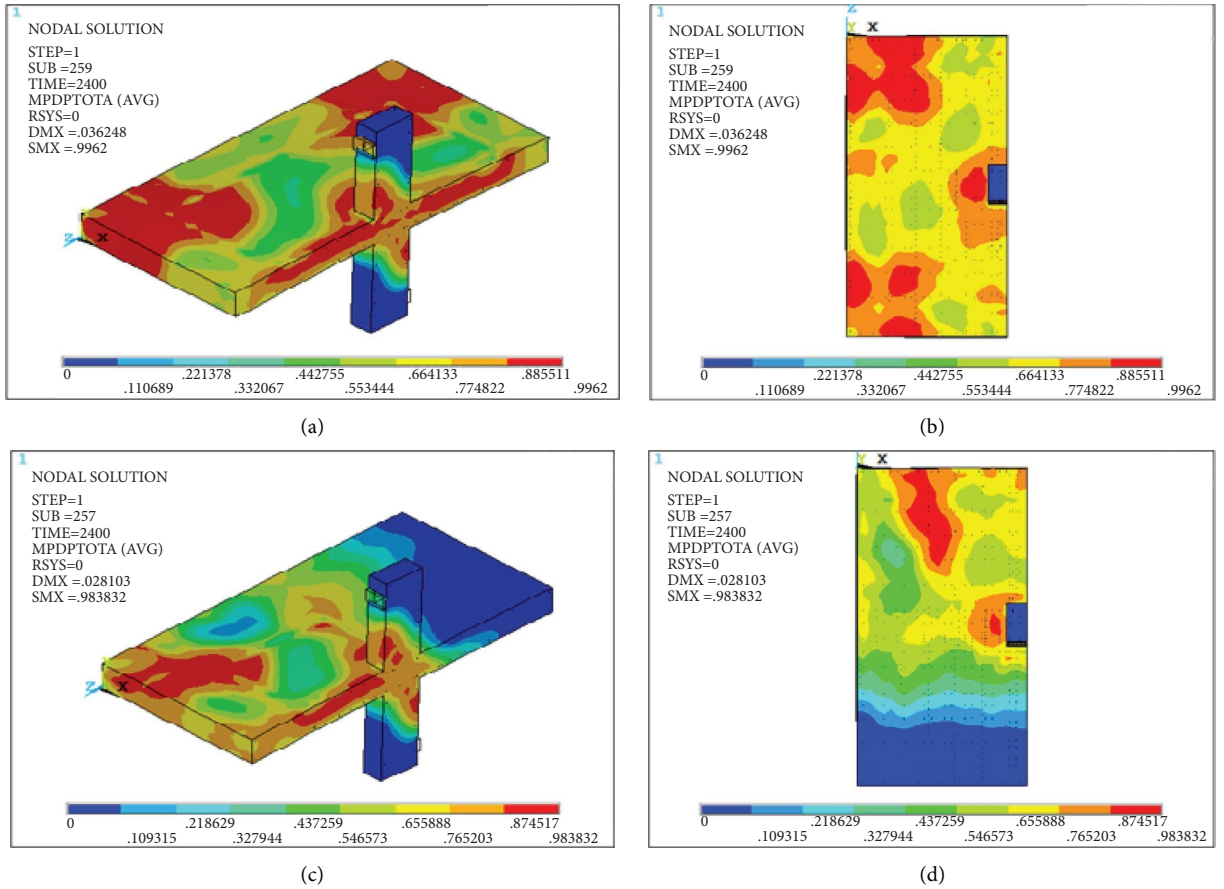

Figure 41: Continued.

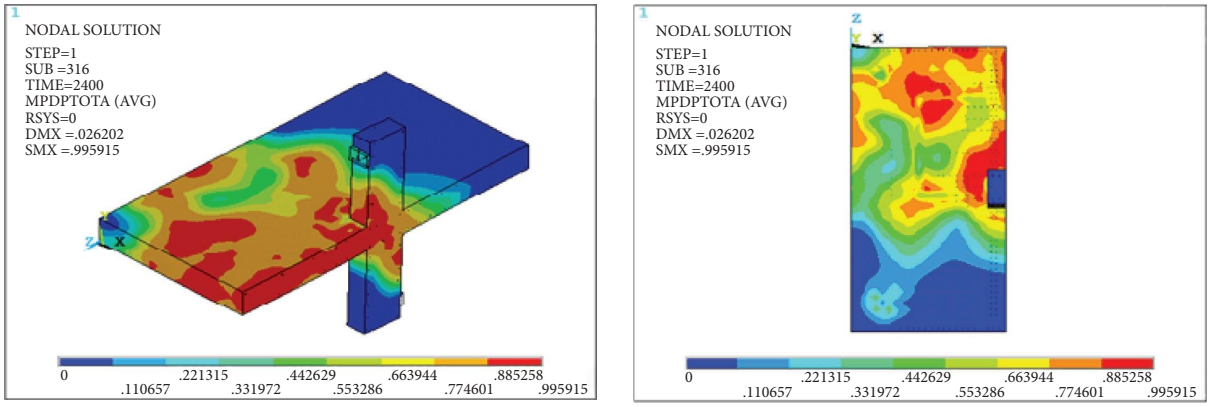

(e) (f)

Figure 41: Concrete damage of specimens with varying fire exposed surface. (a) Specimen 200-45-1-ALL TS-2400. (b) Bottom surface. (c) Specimen 200-45-1-Half TS-2400. (d) Bottom surface. (e) Specimen 200-45-1-Half BS-2400. (f) Bottom surface.

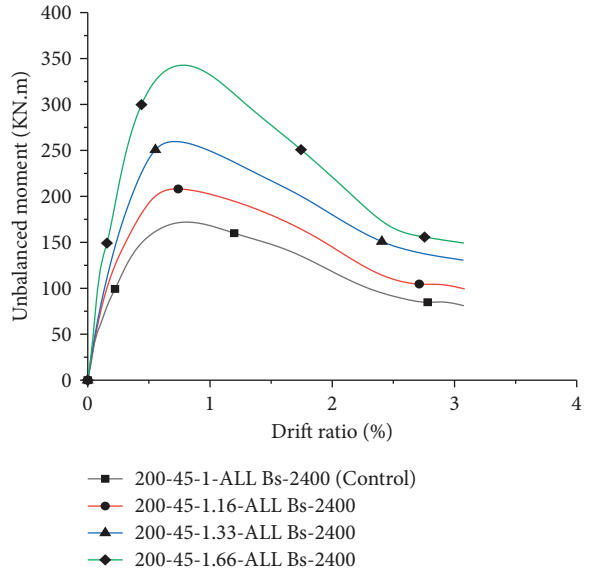

Figure 42: Effect of column aspect ratio on unbalanced moment drift ratio.

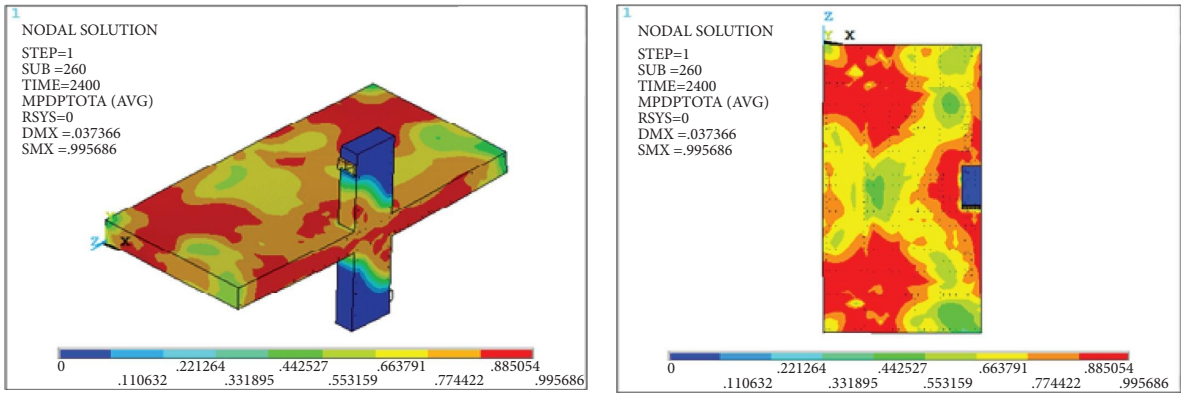

(a) (b)

Figure 43: Continued.

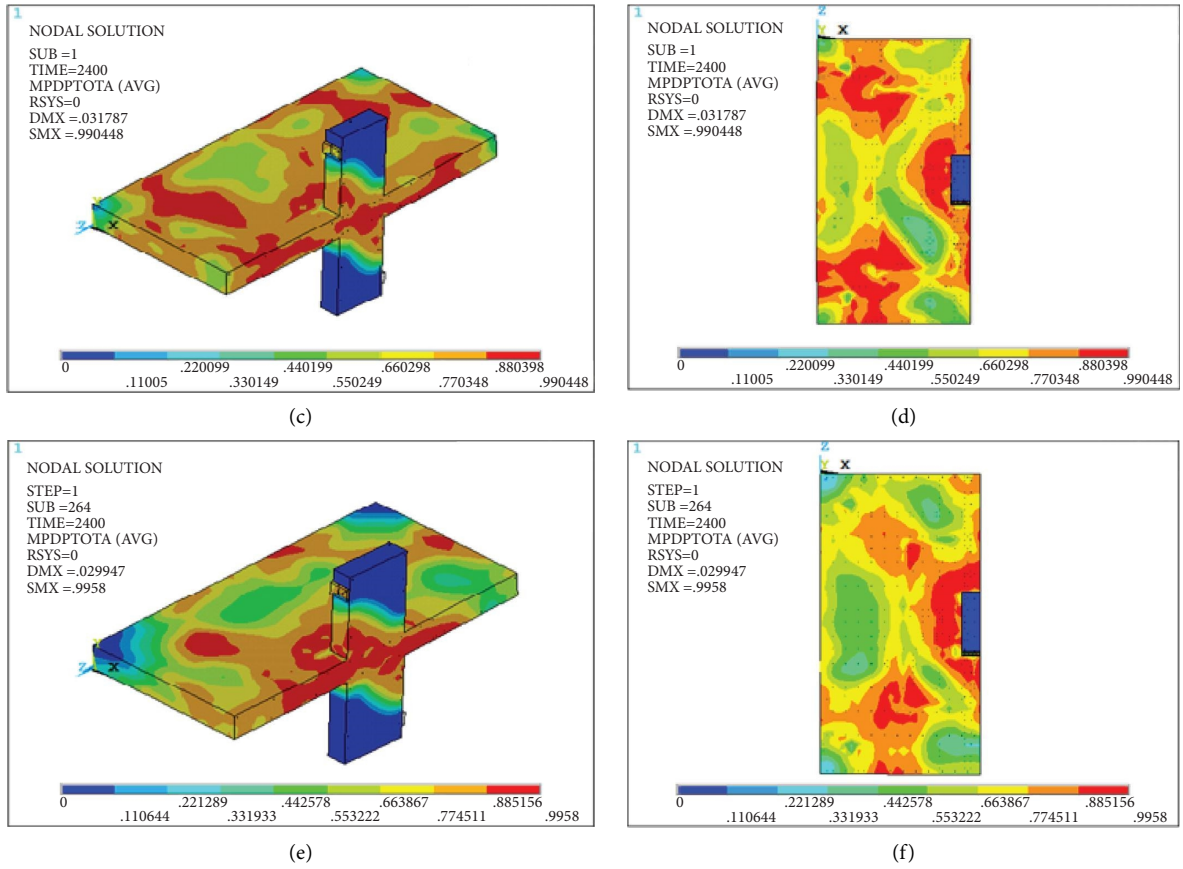

Figure 43: Concrete damage of specimens with varying column aspect ratio. (a) Specimen 200-45-1.166-ALL BS-2400. (b) Bottom surface. (c) Specimen 200-45-1.333-ALL BS-2400. (d) Bottom surface. (e) Specimen 200-45-1.666-ALL BS-2400. (f) Bottom surface.

and 14.29% for specimens with post-earthquake fire exposed surfaces of all top slab surface, half top slab surface, and half bottom slab, respectively. Also, results show that post-earthquake fire exposed to the bottom surface exhibits a higher punching strength structural performance loss than the other two (Figure 40).

Figure 41 presents concrete damage for various post-earthquake fire exposed surfaces. Top surface of slab fire exposure exhibited higher concrete damage than the bottom surface of slab fire exposure. This can be accounted to the lower top reinforcement ratio as compared to the bottom GFRP-reinforcedslab-column connection.

3.2.5. Effect of Column Rectangularity (Aspect Ratio). The column aspect ratio, or rectangularity, is calculated by the ratio of lengths of long and short sides of a column. Column rectangularity would have an impact on the punching capacity of flat plates by reducing the shear stress capacity along the critical perimeter. This hypothesis was tested by considering three different column rectangularity indexes ($\beta = 1.16$, 1.33, and 1.66) on GFRP-reinforcedslab-column connection under post-earthquake fire loading.

FEA results showed that as compared to control ($\beta = 1$), GFRP-reinforcedslab-column connection with column aspect ratios of 300×350 mm ($\beta = 1.16$), 300×400 mm ($\beta = 1.33$), and 300×500 mm ($\beta = 1.66$) exhibited ultimate moments increments of 21.41%, 51.53%, and 99.21%, respectively (Figure 42). Increasing column aspect ratio decreased shear stress capacity along the critical perimeter and pushed failure perimeters away from the column.

Figure 43 presents concrete damages for GFRP-reinforcedslab-column connection models under post-earthquake fire with various column aspect ratio. Column aspect ratio increment has illustrated a higher effect on decreasing concrete damage relative to gains in unbalanced moment drift ratios. This is attributed to column aspect ratio increments lead failure perimeters away from the column, which indirectly lessens concrete damage. However, at an aspect ratio of 1.66, concrete damage increased as compared to others. This can be accounted to the formation of stress concentration at the corner location of the column.

4. Conclusions

In this study, behavior of interior GFRP-reinforcedslab-column connections with GFRP shear reinforcement provided at 2 d from the face of the column under post-earthquake fire was investigated. Influential parameters such as effects of post-earthquake fire exposure duration, concrete grade, slab thickness, post-earthquake fire exposure

surfaces, and column aspect ratio (regularity index) were studied to learn response of on GFRP-reinforcedslab-column connections when subjected to post-earthquake fire.

(i) Post-earthquake fire exposure duration affects the punching shear carrying capacity of GFRP-reinforcedslab-column connections. As compared to the control, post-earthquake fire exposure duration decrement from 1800 seconds to 600 seconds increased the punching shear carrying capacity by 1.89% to 9.58%.

(ii) Concrete grade influences post-earthquake fire punching shear carrying capacity of GFRP-reinforcedslab-column connections. As compared to the control (C45 MPa), decreasing concrete grade from C35 Mpa to C25 Mpa decreased punching shear carrying capacity by −12.18% to −26.77%.

(iii) Slab thickness impacts post-earthquake fire punching shear carrying capacity of GFRP-reinforcedslab-column connections. As compared to control (slab thickness 200 mm), GFRP-reinforcedslab-column connections with slab thickens of 150 mm to 250 mm, improved the punching shear carrying capacity by −22.24% to 22.85%.

(iv) Location of post-earthquake fire exposed surfaces affects response of GFRP-reinforcedslab-column connections. As compared to the control (all slab bottom face post-earthquake fire exposure), post-earthquake fire exposure of all top slab surface, half top slab surface, and half bottom slab surface exhibited 7.74%, 14.18, and 14.29% gain in punching shear carrying of GFRP-reinforcedslab-column connection, respectively.

(v) Among considered parameters, column rectangularity has a higher impact on post-earthquake fire punching shear carrying capacity of GFRP-reinforcedslab-column connections. As compared to the control ($\beta = 1$), increasing column rectangularity from 1.16 to 1.66 resulted in 21.41% to 99.21% gain in punching shear carrying of GFRP-reinforcedslab-column connection.

Data Availability

All data are included in the manuscript.

Conflicts of Interest

The authors declare that they have no conflicts of interest.

Acknowledgments

The authors are grateful to Addis Ababa Science and Technology University for supporting this research.

References

[1] R. K. S. Al Hamd, *Punching Shear in Heated Interior Reinforced Concrete Slab-Column Connections*, The University of Manchester, Manchester, UK, 2018.

[2] M. El-Gendy and E. El-Salakawy, "Effect of flexural reinforcement type and ratio on the punching behavior of RC slab-column edge connections subjected to reversed-cyclic lateral loads," *Engineering Structures*, vol. 200, Article ID 109703, 2019.

[3] M. Eladawy, M. Hassan, B. Benmokrane, and A. Fam, "Effect of stirrups on lateral cyclic behavior of interior glass fiber-reinforcedpolymer-reinforced concrete slab-column connections," *ACI Structural Journal*, vol. 117, 2020.

[4] M. Hassan, E. A. Ahmed, and B. Benmokrane, "Punching shear behavior of two-way slabs reinforced with FRP shear reinforcement," *Journal of Composites for Construction*, vol. 19, no. 1, Article ID 04014030, 2015.

[5] A. Gouda and E. El-Salakawy, "Behavior of GFRP-RC interior slab-column connections with shear studs and high-moment transfer," *Journal of Composites for Construction*, vol. 20, no. 4, Article ID 04016005, 2016.

[6] A. H. Hussein and E. F. El-Salakawy, "Punching shear behavior of glass fiber-reinforcedpolymer-reinforced concrete slab-column interior connections," *ACI Structural Journal*, vol. 115, no. 4, 2018.

[7] M. G. El-Gendy and E. F. El-Salakawy, "GFRP shear reinforcement for slab-column edge connections subjected to reversed cyclic lateral load," *Journal of Composites for Construction*, vol. 24, no. 2, Article ID 04020003, 2020.

[8] M. Eladawy, M. Hassan, B. Benmokrane, and E. Ferrier, "Lateral cyclic behavior of interior two-way concrete slab–column connections reinforced with GFRP bars," *Engineering Structures*, vol. 209, Article ID 109978, 2020.

[9] M. G. El-Gendy and E. El-Salakawy, "Punching shear behavior of GFRP-RC slab-column edge connections," *Special Publication*, vol. 322, pp. 5–1, 2018.

[10] J. H. Wang, S. Kunnath, J. He, and Y. Xiao, "Post-earthquake fire resistance of circular concrete-filled steel tubular columns," *Journal of Structural Engineering*, vol. 146, no. 6, Article ID 04020105, 2020.

[11] H. Salem, H. Issa, H. Gheith, and A. Farahat, "Punching shear strength of reinforced concrete flat slabs subjected to fire on their tension sides," *HBRC Journal*, vol. 8, no. 1, pp. 36–46, 2012.

[12] Ansys, "ANSYS help," 2019, https://www.ansys.com/en-in.

[13] Z. P. Bažant and P. G. Gambarova, "Crack shear in concrete: crack band microflane model," *Journal of Structural Engineering*, vol. 110, no. 9, pp. 2015–2035, 1984.

[14] I. Zreid and M. Kaliske, "Regularization of microplane damage models using an implicit gradient enhancement," *International Journal of Solids and Structures*, vol. 51, no. 19-20, pp. 3480–3489, 2014.

[15] I. Zreid and M. Kaliske, "An implicit gradient formulation for microplane Drucker-Prager plasticity," *International Journal of Plasticity*, vol. 83, pp. 252–272, 2016.

[16] J. A. Purkiss and L.-Y. Li, *Fire Safety Engineering Design of Structures*, CRC Press, Boca Raton, Florida, USA, 2013.

[17] E. N. Bs, *1-2: 2002 Eurocode 1: Actions on Structures—Part 1-2: General Actions—Actions on Structures Exposed to Fire*, British Standards, London, UK, 1991.

[18] W. M. Rohsenow, J. P. Hartnett, and Y. I. Cho, *Handbook of Heat Transfer*, McGraw-Hill, New York, NY, USA, 1998.
[19] C. E. N. Eurocode, *2: Design of Concrete Structures—Part 1–2: General Rules—Structural Fire Design*, European Standard, London, UK, 2004.
[20] E. M. Alawadhi, *Finite Element Simulations Using ANSYS*, CRC Press, Boca Raton, Florida, USA, 2009.
[21] A. Balaji, P. Nagarajan, and T. Madhavan Pillai, "Predicting the response of reinforced concrete slab exposed to fire and validation with IS456 (2000) and Eurocode 2 (2004) provisions," *Alexandria Engineering Journal*, vol. 55, no. 3, pp. 2699–2707, 2016.
[22] M. Saafi, "Effect of fire on FRP reinforced concrete members," *Composite Structures*, vol. 58, no. 1, pp. 11–20, 2002.
[23] Aci, *Guide for the Design and Construction of Structural concrete Reinforced with Fiber-Reinforced Polymer (FRP) bars.(ACI 440.1 R-15)*, ACI, Michigan, USA, 2015.
[24] T. T. Lie, *ASCE Manuals and Reports on Engineering Practice No. 78, Structural Fire protection*, American Society of Civil Engineers (ASCE), New York, NY, USA, 1992.
[25] T. A. Mohammed and T. Alebachew, "Numerical investigation of as-built and carbon fiber reinforced polymer retrofitted reinforced concrete beam with web openings under impact loading," *ASEAN Engineering Journal*, vol. 12, no. 1, pp. 173–182, 2022.
[26] S. Abebe and T. A. Mohammed, "Performance assessment of reinforced concrete frame under close-in blast loading," *Advances in Civil Engineering*, vol. 2022, Article ID 3979195, 24 pages, 2022.
[27] A. R. Mohamed, M. S. Shoukry, and J. M. Saeed, "Prediction of the behavior of reinforced concrete deep beams with web openings using the finite element method," *Alexandria Engineering Journal*, vol. 53, no. 2, pp. 329–339, 2014.
[28] H. Behnam, J. S. Kuang, and B. Samali, "Parametric finite element analysis of RC wide beam-column connections," *Computers and Structures*, vol. 205, pp. 28–44, 2018.